

Award Accounts

The Chemical Society of Japan Award for Young Chemists for 2006

Synthesis of Organic Shell–Inorganic Core Hybrid Nanoparticles by Wet Process and Investigation of Their Advanced Functions

Mami Yamada

Department of Applied Chemistry, Tokyo University of Agriculture and Technology (TAT), 2-24-16 Nakacho, Koganei, Tokyo 184-8588

Precursory Research for Embryonic Science and Technology (PRESTO), Japan Science and Technology Agency (JST), 4-1-8 Honcho, Kawaguchi 332-0012

Received July 16, 2008; E-mail: m-yamada@cc.tuat.ac.jp

This account reviews the chemical synthesis of inorganic nanoparticles stabilized by an organic shell layer and the investigation of their specific characteristics. Consideration of design and construction of organic–inorganic hybrid nanoparticles by wet process is indispensable in order to exploit the unprecedented nature resulting from the fusion of both organic and inorganic traits. In a series of studies, two synthetic parameters were the center of focus: physical construction of the inorganic core and the chemical constituents introduced. External stimuli such as electric fields or solvent polarity can be utilized to transform the characteristics of nanoparticles when redox active or liquid crystalline molecules as an organic shell are attached to the surface of an inorganic nano-core. In another case, the catalytic activities of nanoparticles are controllable by modifying the crystal faces and the surface area of the inorganic cores in connection with shape and size. Novel nanomaterial has also been fabricated by choosing a metal coordination polymer as a core, leading to the first isolation of alkyl chain-stabilized metal coordination nano-polymers (MCNPs). The compounds are listed as Pt nano-cubes, size-selected Au nanoparticles, metal hexacyanoferrate MCNPs, and metal nanoparticles functionalized by biferrocene, anthraquinone, and triphenylene derivatives. Synthetic procedures and remarkable characteristics are demonstrated.

Introduction

Nanometer-sized inorganic compounds consisting of several hundred to several thousand atoms, serve as particulate material which exhibit specific physical properties different from discrete molecules and solid-states.[1,2] In the 1800s, Faraday prepared a red solution which was made from small gold colloid sol.[3] By microminiaturization, surface plasmon resonances (vibration of a free electron) are enhanced,[4] resulting in the gold, which shows metallic luster as a bulk crystal, displaying a transparent red color. Another example is that when the crystal size of silicon is reduced to a nanometer scale, it starts to emit ultraviolet or visible light depending on the size.[5] The above phenomena originate from surface effects and quantum size effects. Because of these effects nanoparticles show promise as efficient catalysts with high surface area,[6] highly-sensitive biosensors,[7] new optical units,[8] high-density magnetic media,[9] and many other applications. Overall, development of synthetic methods, properties, and applications of nanoparticles has been remarkable.[10] Among these areas, synthesis is the fundamental basis for manipulating particle properties through control of the ratio of components and physical construction. The preparation of nanoparticles can be carried out in three different phases: solid, gas, and solution phase. Generally, solid- and gas-phase methods need a large-scale apparatus for pulverization, vacuum evaporations, or laser ablation of inorganic bulk crystals, while a wet process in solution phase can be performed in a simple glass implement. Solution-phase synthesis takes what is called a bottom-up approach by rendezvous of inorganic atoms (ions) to a nanometric particle, and is considered to have potential for fabricating unprecedented nanoparticle materials with novel chemical and physical structures by selecting various synthetic parameters.

Usually, nanoparticles obtained by the solution process are inorganic nanometer-sized crystals protected by an organic layer as an organic-shell inorganic-core structure. The organic shell contributes to high stability of nanoparticles which can prevent denaturation such as oxidation and aggregation of particles. In addition, the surface protection enables the isolation of nanoparticles in air as a powder after solvent evaporation. The obtained nanoparticles can be redispersed into a solvent, which is anticipated to afford processibility for practical use.

As a forerunner in solution process research, the Au_{55} particle reported by Schmid et al. in 1981 should be mentioned.[11]

Published on the web February 13, 2009; doi:10.1246/bcsj.82.152

The synthesis was carried out in the presence of triphenylphosphine as an organic shell by diborane reduction of Au ions. The melting point depression and the specificity of the electronic state were discussed. Subsequently, the introduction of Pd atoms was also investigated.[12] Toshima et al. demonstrated the synthesis of Pt nanoparticles protected by a polymer, and showed their catalytic function.[13] Convenient and large-scale synthesis of Au nanoparticles was reported by Brust et al.,[14] and subsequently, synthetic studies in solution have been increasing exponentially. In the 1990s, noble metals other than gold and platinum (Pd, Ru, Cu, Ag, etc.)[15] and their alloys,[16,17] were investigated as inorganic cores. In 2000, the introduction of sulfide, oxide materials like CdS[18] and Fe_2O_3,[19] and various metals which were more easily oxidized compared to noble metals e.g., Fe,[20] Co,[21] Si,[22] and NiAl,[23] began to be energetically investigated. Furthermore, the use of 3D metal coordination polymers as a core material were newly illustrated.[24]

As noted above, the range of inorganic substances which can be utilized as core components has expanded. Simultaneously, wet synthesis has been progressing both in terms of controlling physical structure and hybridization of organic and inorganic materials to give unique functions. The synthesis of particles with a very narrow size distribution is achieved by control of nucleation and nuclear growth of nanoparticles in solution. At present nanoparticles with a size distribution below several percent can be prepared with various metals.[25] In order to control shape, synthetic parameters are particularly important. Temperature, time, the organic ligand, and free energy change (ΔG) must be taken into consideration in order to achieve precise structural control.[26] Precision synthesis has enabled the preparation of forms such as rods, cubes, tetrahedrons, and tetrapods.[27] Reports of hybrid nanoparticles have been considerable. Mirkin et al. introduced DNA–thiol derivatives into a water-soluble Au nanoparticle surface.[7] Murray et al. reported the immobilization of redox ferrocene (Fc) species on gold nanoparticles.[28] Since then the introduction of versatile functional organic molecules, e.g., multiple redox,[29] photoactive,[30,31] radical,[32] and polymer's monomer,[33] have been reported. By hybridization, multiple properties originating in both the surface organic molecules and the inorganic core are expressed and the variation could be possibly utilized.

Against the backdrop noted above, this account presents the nanoparticle research carried out by the author under the primary theme of "fabrication of organic-shell inorganic-core hybrid nanoparticles designed by wet process and investigation of their advanced functions." There exist numerous patterns to select components for organic and inorganic composites. In general, an organic material excels in the versatility of its physical structure including flexibility, while inorganic material can accumulate multiple electrons forming various electronic states. The properties of nanoparticles, which depend on their material parameters (e.g., physical structure, elemental ratio, and organic/inorganic hybridization effects) are not completely understood. For overall elucidation of wet process nanoparticle science, preparation of newly compounded nanoparticles by controlling unit selection, physical structure, and component ratio is indispensable. Through feedback from the experimental information gathered on the basis of these research concepts, the series of studies presented here aim to show the preparation of novel organic/inorganic nanoparticles with functions including electrochemical, optical, catalytic, and magnetic properties. The examined nanoparticles have been classified into three groups: (1) functionalized organic molecules-attached metal nanoparticles, (2) shape- and size-controlled metal nanoparticles, and (3) nanometer-sized metal coordination polymers. These topics are illustrated in connection with the author's publications.

1. Metal Nanoparticles Functionalized by Organic Molecules

In the first section, functional-molecule-modified noble metal nanoparticles are presented, which have prominent properties originating from the combination of the inorganic metal core and organic shell. Functionalization based on a metal core will open an unexpected interesting avenue to examine intra- and intermolecular nanoparticle chemistry and to design new photoelectrochemical systems, multi-step, highly catalytic, and electron donor/acceptor reactions using nanoparticles. The fundamental method to functionalize metal nanoparticles was thiol-exchange reaction between an alkylthiolate on a particle surface and thiol derivatives with functional organic molecules.[28] The method is easy and can be utilized for various nanoparticle functionalizations. It can also be used to make poly-functionalized metal nanoparticles by means of particles modified with mixtures of different thiols. The reactivity of thus prepared metal nanoparticles should be investigated for further synthetic steps and the development of novel functions.[34–36] In this section, as functional molecules, redox-active units (biferrocene and anthraquinone) and a liquid crystal molecule (triphenylene) are selected. The characteristics of the prepared organic–inorganic nanoparticles could be controlled by the physical and chemical state of the surrounding functional species with outside stimulation i.e., applied electronic field and dielectric strength around the particles.

1.1 Multiple-Redox Species-Modified Metal Nanoparticles. 1.1.1 Electrochemical Assembly of Biferrocene-Attached Gold Nanoparticles (Au_n–BFc): Multinuclear complexes with metal–metal electronic interaction exhibit unique optical and magnetic properties which have been studied for decades, e.g., π-conjugated ethylenedithiolato complexes[37] and oligoferrocenylene.[38] The concept of combining electron-rich multinuclear complexes with metal nanoparticles would be a good model to understand a new multiple electron transfer system. Here, biferrocene (BFc) is selected as a multinuclear complex, which undergoes a two-step one-electron oxidative reaction of $BFc/BFc^+/BFc^{2+}$ in electrolyte solution. A high charge accumulation at the particle/solution interface is expected under applied electronic field when BFc units are attached to a particle surface. BFc-modified gold nanoparticles (Au_n–BFc) were synthesized by a thiol exchange between octanethiolate-stabilized metal nanoparticles (Au_n–OT) and a BFc thiol derivative, biferrocen-1′-yl 8-mercaptooctyl ketone (BFcS) (Scheme 1).[29,39] Generally, stable gold nanoparticles stabilized by thiolates are obtained by the reduction of Au^{III} ions ($HAuCl_4$, $AuCl_3$, etc.) in solution with a surface active agent (TOAB, DDAB, etc.), a reducing agent ($NaBH_4$, Super Hydride, etc.), and an alkyl thiol with

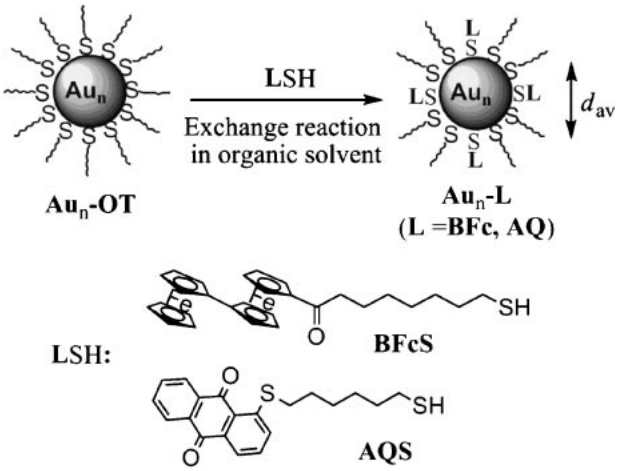

Scheme 1. Preparation of Au_n–BFc and Au_n–AQ.

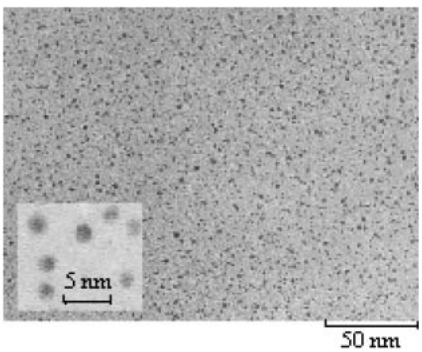

Figure 1. TEM image of Au_n–BFcs ($d_{av} = 2.3$ nm, $\theta_{BFc} = 7.5$).

appropriate chain length.[14,25,40] The average gold core diameter in Au_n–OTs, d_{av}, changed in the range of 1.5–8.0 nm depending on the parameters, mainly the molar ratio of Au ions to the octane thiolate.[40] The number of exchanged BFcS on the Au_n–OT surface, θ_{BFc}, was calculated based on the ratio of the integrals of the ^{1}H NMR signals between BFc (2.9–4.7 ppm) and methyl protons (0.8–0.9 ppm). The value of θ_{BFc} varied with the molar ratio of Au_n–OT to BFcS during the exchange reaction. Figure 1 shows a transmission electron microscopy (TEM) image of Au_n–BFcs with $d_{av} = 2.3$ nm and $\theta_{BFc} = 7.5$).[39] It is seen that the nanoparticles are individually isolated by stable organic shells. Au_n–BFcs could be obtained as a black powder after alcohol purification, however, they were easily redispersed into several organic solvents e.g., CH_2Cl_2, chloroform, THF, and hexane due to the hydrophobic nature of the organic shell.

Figure 2a shows a typical cyclic voltammograms (CVs) of Au_n–BFcs, which is measured at an indium tin oxide (ITO) electrode in electrolyte solution of Bu_4NClO_4–CH_2Cl_2. The peak current increases gradually with consecutive potential scans between −0.3 and 0.9 V vs. Ag/Ag^+ where two-step $1e^-$ oxidation due to BFc units on the particle surface occurs at 0.20 and 0.61 V vs. Ag/Ag^+, suggesting that Au_n–BFc particles flock on an electrode/solution interface by 2 electron oxidation of BFc sites. UV–vis spectra of Au_n–BFc films thus prepared exhibit broad absorption bands that grow in intensity with

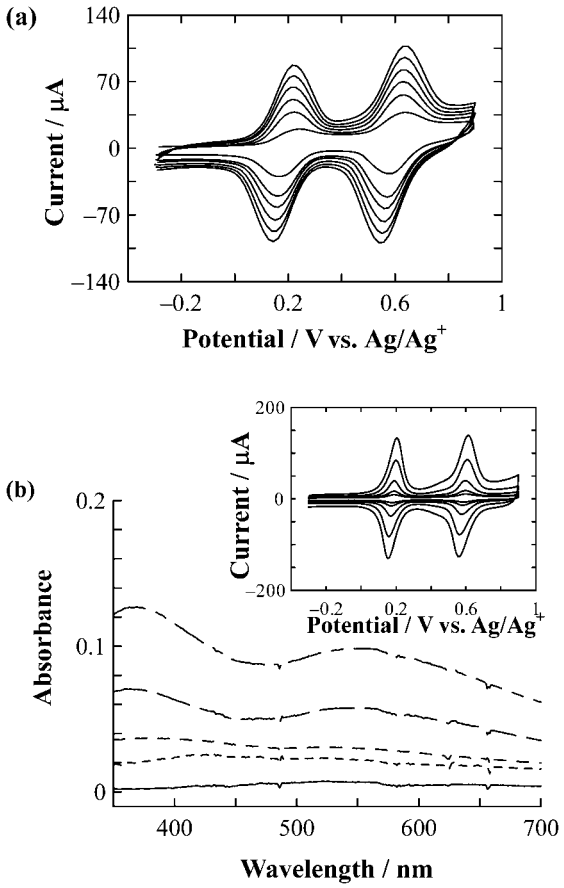

Figure 2. (a) Cyclic voltammograms of 1.7 μM of Au_n–BFc ($d_{av} = 2.9$ nm, $\theta_{BFc} = 20.8$) at ITO in 0.1 M Bu_4NClO_4–CH_2Cl_2 at 100 mV s^{-1} between −0.3 and 0.9 V vs. Ag/Ag^+ in the positive direction at the 1st, 10th, 20th, 30th, 40th, and 50th cyclic scan, as shown from the bottom of the figures to the top. (b) UV–vis spectra and (inset) cyclic voltammograms in 0.1 M Bu_4NClO_4–CH_2Cl_2 of the electrodeposited Au_n–BFc films prepared under the same conditions as Figure 2a with 3, 10, 25, 50, and 75 cyclic scans, as shown from the bottom of the figure to the top (Ref. 40).

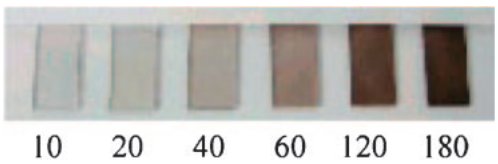

Figure 3. Photographs of electrodeposited Au_n–BFc films prepared in a solution of 5.0 μM Au_n–BFc ($d_{av} = 2.3$ nm, $\theta_{BFc} = 15$) at ITO 0.1 M Bu_4NClO_4–CH_2Cl_2 at 100 mV s^{-1} between −0.3 and 0.9 V vs. Ag/Ag^+. The numbers in the figure are those of the cyclic scans (Ref. 39).

increasing number of potential scans (Figure 2b), meaning that the thickness of the film is controlled by changing the number of potential scans. Figure 3 displays the actual photographs of the Au_n–BFc films on ITO, which confirms that the black deposition due to Au_n–BFc is tightly attached onto a transparent ITO electrode. CVs of the electrode films in pure electrolyte solution show two pairs of cathodic and anodic

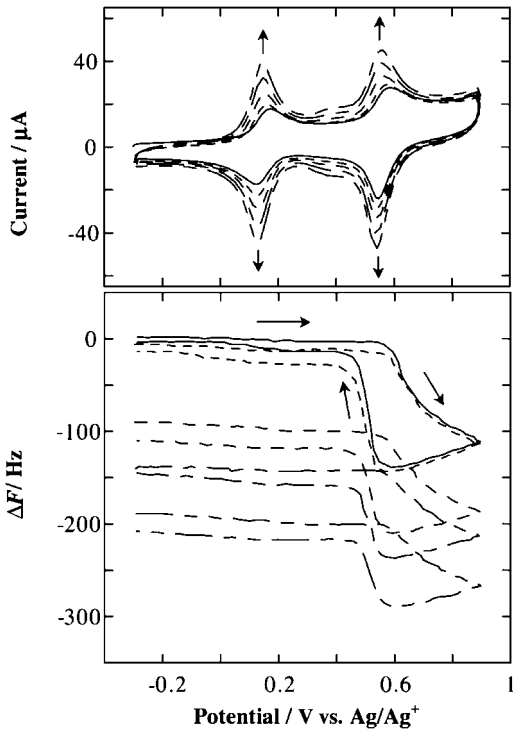

Figure 4. Cyclic voltammograms (top) and ΔF-potential curves (bottom) of 5.2 μM Au_n–BFc ($d_{av} = 2.3$ nm, $\theta_{BFc} = 7.5$) at a gold electrode in 0.1 M Bu_4NClO_4–CH_2Cl_2 at 100 mV s^{-1} between −0.3 and 0.9 V vs. Ag/Ag^+ in the positive direction with the 1st (solid line), 5th (dotted line), 10th (dashed line), 15th (dot-dashed line), and 20th (2-dot-dashed line) scans (Ref. 39).

waves (Figure 2b, inset), the peak currents of which are proportional to the potential scan rate, indicating the behavior of surface immobilized BFc species in the film. The construction of Au_n–BFc films with a different value of d_{av} was applicable by using the same electrodeposition process, independent of the core size.[40]

The electrodeposition mechanism was analyzed by electrochemical quartz crystal microbalance (EQCM) measurement. Figure 4 displays the typical EQCM behavior of Au_n–BFcs at a gold electrode in Bu_4NClO_4–CH_2Cl_2. In the first potential sweep in the positive direction, only a slight frequency decrease is observed in the first electron oxidation of the BFc moieties at $E_1^{0\prime} = 0.15$ V, whereas the frequency decreases dramatically from 0.54 to 0.9 V when the second electron oxidation of the BFc sites takes place at $E_2^{0\prime} = 0.54$ V. This behavior reflects that the electro-oxidative aggregation of Au_n–BFcs occurs by $2e^-$ oxidation of the BFc units, since a frequency decrease relates to a mass increase on the electrode. This phenomenon is consistent with the fact that electrodeposition was not reported for single nuclear Fc-functionalized Au nanoparticles.[28] It can be said that the introduction of a multi-redox system is necessary to activate the formation of metal nanoparticles. When the BFc units are oxidized to BFc^{2+} the ionic atmosphere around the gold cores become thicker through the production of ionic bonding between BFc^{2+} units and electrolyte anions in solution. Consequently, the collective interaction among the Au_n–BFcs including the electrostatic

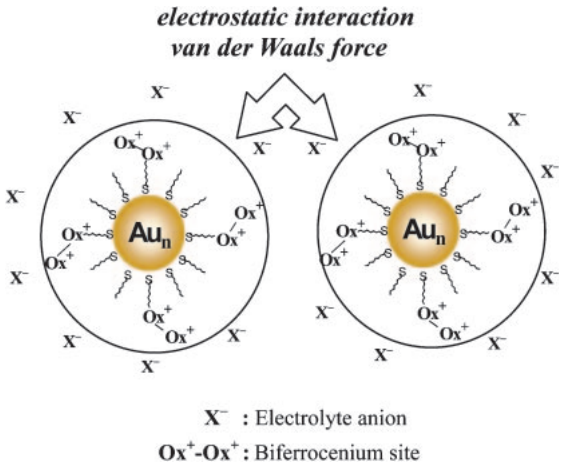

Figure 5. Illustration of collective interaction between adjacent Au_n–BFcs by electro-oxidation.

interaction and the van der Waals force becomes larger accompanied by decrease of solvation, leading to the electrochemical assembly of Au_n–BFcs (Figure 5).

Subsequently, when the potential scan is reversed at 0.9 V to negative potential, the frequency continues to decrease until 0.54 V, however a significant frequency increase starts after the electrode potential becomes more negative than $E_2^{0\prime}$. The frequency difference before and after the potential cycling at −0.3 V corresponds to the net weight of the deposited Au_n–BFcs. For example, a frequency decrease of 6.0 Hz after the first scan corresponds to 9.7×10^{-8} g increase in mass calculated by the Sauerbery equation[41] of $\Delta F = -C \times \Delta W$, where ΔF is the frequency change, C is the proportional constant that depends on the parameters of QCM electrode properties (e.g., the electrode area, quartz density, and quartz elasticity, and the value is equivalent to 6.17×10^7 Hz g^{-1} in this study), and ΔW is the weight change of the electrode. During the course of repeated cyclic potential scans, similar ΔF-potential behavior in one cycle was observed, and the frequency steadily decreased after each cycle with current increase of cyclic voltammograms, indicating that the Au_n–BFc layer is continuously accumulated on the electrode surface.

These EQCM results summarize the electrodeposition mechanism of Au_n–BFcs as follows: 1) Au_n–BFcs are apt to aggregate at the electrode/electrolyte interface and adsorb to the electrode by the formation of BFc^{2+} on the particle surface, 2) significant desorption of assembled Au_n–BFcs from the electrode occurs after BFc sites are returned to the neutral state by reduction, and 3) a small portion of the strongly adsorbed flocks of Au_n–BFcs remain on the electrode. By repeating the potential scans, the Au_n–BFc film might be fabricated by the remaining adsorbed Au_n–BFcs, resulting in formation of the nanoparticle domains (see below).

The morphological features of the Au_n–BFc film on HOPG were examined by STM and AFM as shown in Figure 6. The STM image completely covered the electrode surface forming the particle film which is flat within a level of 5 nm in height (Figure 6a). The average spacing between the adjoining electrodeposited Au_n–BFcs was measured as 7.5 nm. This value is larger than the estimated maximal Au_n–BFc particle

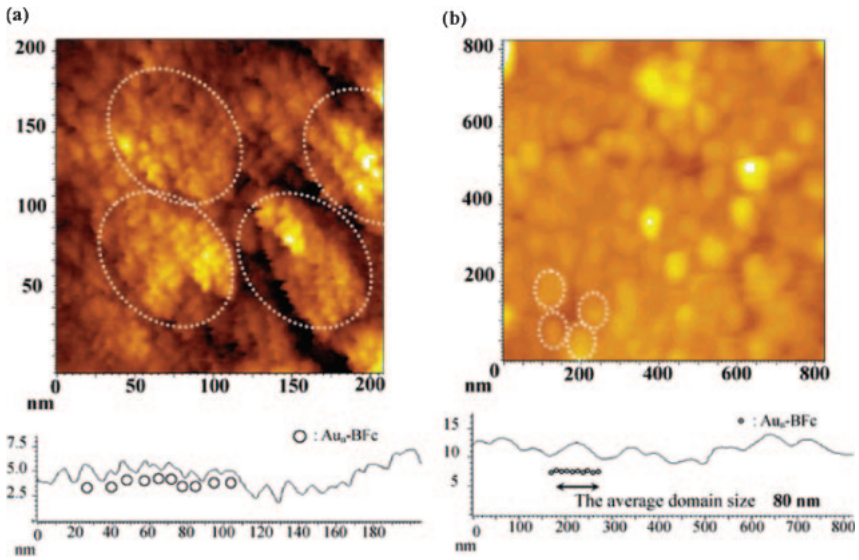

Figure 6. (a) STM and (b) AFM images of the Au_n–BFc film prepared in a solution of 5.2 μM Au_n–BFc ($d_{av} = 2.3$ nm, $\theta_{BFc} = 7.5$) at HOPG with 5 cyclic scans in 0.1 M Bu_4NClO_4–CH_2Cl_2 at 100 mV s^{-1} between −0.3 and 0.9 V vs. Ag/Ag^+ in the positive direction, and the typical cross-sectional profile along the cross axis (Ref. 39).

size of 5.9 nm (core diameter, 2.3 nm; octyl thiolate, 1.0 nm; and biferrocene, 0.8 nm) even if a deviation in core diameter of 0.5 nm is taken into consideration. This is attributed to the counter electrolytes (here ClO_4^- anions) which are immobilized among the neighboring BFc units during the deposition process. The introduction of electrolyte anions into the Au_n–BFc film was anticipated by considering the electrodeposition mechanism by EQCM noted above, however it could be confirmed by other experiments using different electrolyte anions (ClO_4^-, BF_4^-, and PF_6^-).[39] Namely, larger electrolyte anions reduce the electrodeposition rate of Au_n–BFcs, meaning that the van der Waals force among the adjacent Au_n–BFc^{2+} nanoparticles decreases with increasing interparticle space by larger anions. The existence of boron in the Au_n–BFc film prepared in Bu_4NBF_4–CH_2Cl_2 was conveniently detected by prompt γ-ray neutron activation analysis (PGA).[39]

In Figure 6a, it is also apparent that domains of particles ca. 70–80 nm in diameter (encircled by a dotted line) are constructed. The AFM image of the same sample in Figure 6b reveals the peculiar nano structure of the Au_n–BFc film; round-shaped domains spreading on the whole surface as if huge particles are assembled on the electrode. The cross-sectional profile demonstrates that the domain size is fairly uniform, with an average diameter of ca. 80 nm, corresponding to ca. 100 Au_n–BFc particles assuming that Au_n–BFcs are packed with a spacing of 7.5 nm. It should be noted that the morphology of the Au_n–BFc film was dependent on the solvent used (CH_2Cl_2, toluene/MeCN, and THF).[42]

1.1.2 Electrooptical Properties of the Au_n–BFc Films: Noble metal nanoparticles e.g., gold, silver, and copper are well known to exhibit a strong broad absorption band in a visible region called the surface plasmon (SP) band. The SP band originates from a coherent oscillation of the conduction electrons in response to optical excitation and the resonance is absent in an individual atom as well as in bulk metal. This phenomenon was first elucidated theoretically by Mie who solved Maxwell's equation for the absorption and scattering of electromagnetic radiation by spherical particles. The spectroscopic changes of the SP band depend on several parameters e.g., core size,[43] chemical adsorbate on the particle surface,[44] surrounding solvent,[45] and core charge,[46] of which aspects can be explained by frameworks applying the Mie theory.[47] As further interpretation, attention should be paid to the "collective" SP band of the metal nanoparticles assembled in the matrix where the particle–particle interactions are included.[48] The prepared Au_n–BFc films exhibited a typical SP band ca. 550 nm influenced by the dipole–dipole coupling among the adjacent particles. It was found that this collective SP band of the Au_n–BFc films offered special electrooptical features different from a single isolated nanoparticle.[49]

Figure 7 illustrates the UV–vis spectral change of the Au_n–BFc film ($d_{av} = 6.4$ nm, $\theta_{BFc} = 4.6$) by applied potential. The λ_{max} value due to the SP band at 584 nm is shifted extremely to a shorter wavelength by 74 nm with increasing absorbance by potential in the negative direction to −1.6 V. On the contrary, the positive potential shift to 1.6 V gives a longer λ_{max} by 8 nm with decreasing absorbance. From these specific changes it can be deduced that the direct charging of electrons in the gold core of Au_n–BFc is predominant compared to the charge accumulation at the immobilized BFc units, because the λ_{max} shift in the negative potential is significantly larger than that in the positive direction where redox reaction of BFc moities occurs.

The analyzed electroscopic data are summarized in Table 1. For instance, the number of electrons provided per particle by charging from 0 to −1.6 V vs. Ag/Ag^+ for the Au_n–BFc films ($d_{av} = 6.4$ nm, $\theta_{BFc} = 4.6$) is estimated to be $42e^-$, based on the consideration that consecutive single-electron transfer processes with the potential spacing (ΔV) are dependent upon the capacitance (C_{core});[50] $\Delta V = e/C_{core}$. It is calculated that $C_{core} = 4.2$ aF by the equation; $C_{core} = 4\pi\varepsilon\varepsilon_0 r(r + d)/d$ where ε is the monolayer dielectric constant, r is the core radius, and d is the monolayer thickness. Assuming that the shift in the SP

Table 1. Spectroelectrochemical Data of the Au_n–BFc Films (Ref. 49)

Particle diameter /nm	C_{core}[a] /aF	ΔV[b] /V	Number of injected electrons to the core[c]	λ_{init}[d] /nm	λ_{final}[d] /nm	$\lambda_{final.ideal}$[e] /nm	$\Delta\lambda_{ex}$[f] /nm	$\Delta\lambda_{ideal}$[g] /nm
2.3	1.1	0.15	$11e^-$	587	574	577	13	10
4.3	2.8	0.057	$28e^-$	604	569	601	35	3
6.4	4.2	0.038	$42e^-$	584	510	582	74	2

a) The core capacitance: $C_{core} = 4\pi\varepsilon\varepsilon_0 r(r+d)/d$ where ε is the monolayer dielectric constant, r is the core radius, and d is the monolayer thickness. b) The potential spacing of consecutive single-electron transfer processes: $\Delta V = e/C_{core}$ c) Electron provision from 0 to −1.6 V calculated by the value of ΔV. d) See Figure 20 at 0 (λ_{init}) and −1.6 V (λ_{final}). e) The value calculated by $\lambda_{final.ideal}/\lambda_{init} = (N_{init}/N_{final})^{1/2}$ where N_{init} and N_{final} are the numbers of free electrons per metal core before and after the charging, respectively, referred to Table 1. f) $\Delta\lambda_{ex} = \lambda_{init} - \lambda_{final}$ g) $\Delta\lambda_{deal} = \lambda_{init} - \lambda_{final.ideal}$.

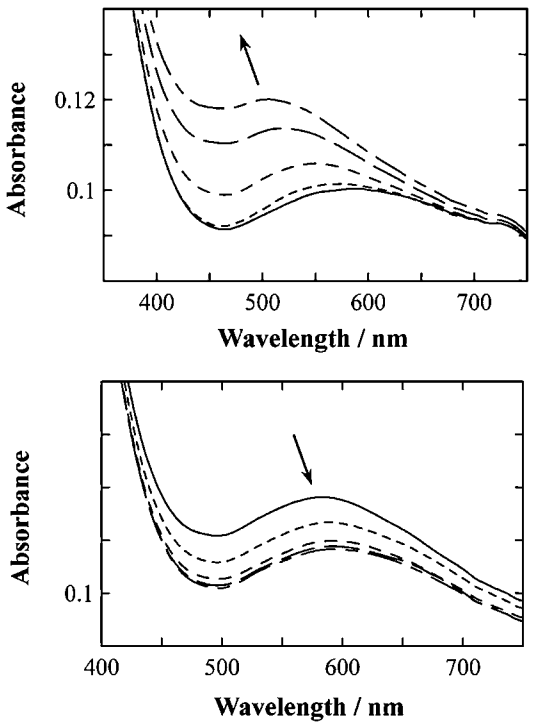

Figure 7. (Top) UV–vis spectra of the Au_n–BFc film ($d_{av} = 6.4$ nm, $\theta_{BFc} = 4.6$) on ITO at given potentials of 0, −0.4, −0.8, −1.2, and −1.6 V vs. Ag/Ag^+ in 0.1 M Bu_4NClO_4–CH_2Cl_2 in the negative direction, and (bottom) at given potentials of 0, 0.4, 0.8, 1.2, and 1.6 V vs. Ag/Ag^+ in 0.1 M Bu_4NClO_4–CH_2Cl_2 in the positive direction (Ref. 40).

band position has occurred only by the charge difference in the metal core, the final SP band position (λ_{final}) at −1.6 V after 42-electron provision from −0 V vs. Ag/Ag^+ is predicted at 582 nm by the convenient equation; $\lambda_{final}/\lambda_{init} = (N_{init}/N_{final})^{1/2}$ where λ_{final} and λ_{init} (=584 nm) are the SP band positions after and before the redox reaction of metal core, respectively, and N_{final} and N_{init} are the numbers of free electrons per metal core after and before the charging, respectively. The experimental value of a 74 nm shift is enormously enlarged compared to this theoretical value of a 2 nm shift. This should be due to the simplification of the adopted equations that the particles exist individually in solution, and the collective SP band shift by applied potential should be explained including dipole–dipole interactions among particles. In Table 1, this particle–particle interaction works more effectively in the Au_n–BFc film with larger particle size, considering that the shifts grow with increasing particles core size. It is interesting that the order of the ideal amount of λ_{max} shift is opposite to the experimental values; namely, the theoretical equations noted above predict that the SP band position of the isolated particles are stimulated more easily with smaller core size by applied potential. From these results it can be deduced that the collective SP band is shifted particularly with interparticle interaction in an entirely different manner than a single particle. It should be noted that the solvent refractive index effect on the collective SP band of the Au_n–BFc film was also specific, which could not be explained by the theoretical equations relating to single metal nanoparticles.[51]

1.1.3 Electrochemical Assembly of Anthraquinone Attached Gold Nanoparticles (Au_n–AQ): Another multiple redox unit, an anthraquinone (AQ) thiol derivative 1-(1,8-dithiaoctyl)anthracene-9,10-dione (AQS)[52] was introduced onto a gold nanoparticle to produce Au_n–AQ ($d_{av} = 2.2$ nm, $\theta_{AQ} = 26$) (Scheme 1).[51,53] BFc and AQ are both multiple redox species, however they are complementary opposites. Namely, the former undergoes two-step one-electron oxidative reaction of $BFc/BFc^+/BFc^{2+}$, while the latter receives two-step one-electron reductive reaction of $AQ/AQ^-/AQ^{2-}$. From the results noted above, the 2 electron oxidation process of BFc units of Au_n–BFc led to the formation of a uniform BFc-active gold nanoparticle film on an electrode. On the contrary, Au_n–AQ is found to be aggregated by 2 electron reduction of AQ sites, clarifying that metal nanoparticles functionalized with multiple-redox molecules could assemble by charge accumulation of redox species on a particle/solution interface. Figure 8 shows the STM images of the Au_n–AQ film. The partial tetragonal-like aggregation is observed. The cross-sectional view of the figure indicates that the separation between the peaks of the curve is 8.5 nm, the value of which is much larger than the estimated maximal Au_n–AQ value of 5.8 nm (the core diameter, 2.2 nm; octyl thiolate, 1.0 nm; and anthraquinone, 0.8 nm). A long inter-cluster distance similar to the Au_n–BFc film (Figure 6) was observed. This result supports the electrodeposition mechanism in this system that the counter cation Bu_4N^+, in the case of the Au_n–AQ film, gathers around the negatively charged AQ units on the surface of the Au_n–AQ, acting as a spacer between adjacent Au_n–AQ of the film.

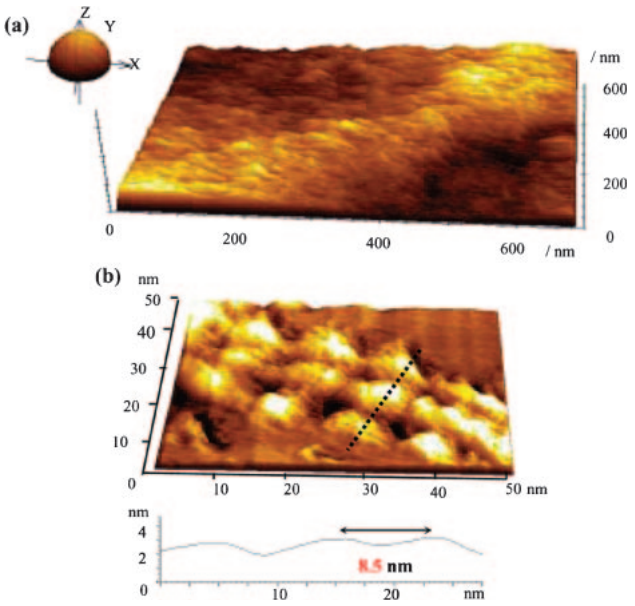

Figure 8. (a) STM image of a multilayer Au_n–AQ ($d_{av} = 2.2$ nm, $\theta_{AQ} = 26$) film electrodeposited on HOPG in the area of $700 \times 700\,nm^2$. (b) STM image of a submonolayer Au_n–AQ film on HOPG in the area of $50 \times 50\,nm^2$ with the cross-sectional profile along the solid line (Ref. 51).

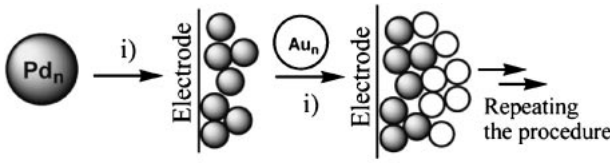

i) Electro-oxidation of biferrocene units on the particle surface in 0.1 M Bu_4NClO_4-CH_2Cl_2

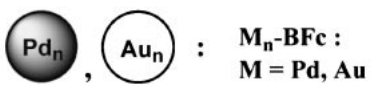

Scheme 2. Preparation of the Au_n–BFc and Pd_n–BFc composite film (Ref. 56).

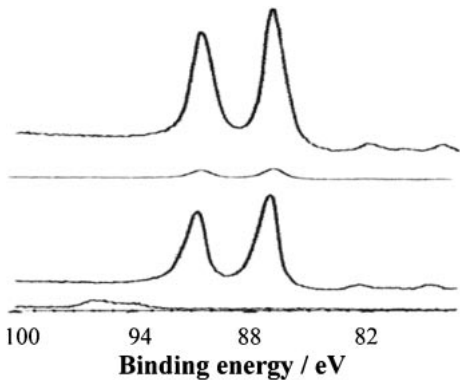

Figure 9. XPS spectra of Pd_n–BFc, Pd_n–BFc/Au_n–BFc, Pd_n–BFc/Au_n–BFc/Pd_n–BFc, $[Pd_n$–BFc/Au_n–BFc$]_2$, $[Pd_n$–BFc/Au_n–BFc$]_2Pd_n$–BFc films, as shown from the bottom of the figure to the top. The films were prepared with 25 cyclic potential scans between −0.3 and 0.9 V vs. Ag/Ag^+ for each metal nanoparticle film in a solution of 3.2 μM Pd_n–BFc ($d_{av} = 3.8$ nm, $\theta_{BFc} = 26.3$) or Au_n–BFc ($d_{av} = 2.9$ nm, $\theta_{BFc} = 20.8$), at ITO in 0.1 M Bu_4NClO_4–CH_2Cl_2 at 100 mV s^{-1} (Ref. 56).

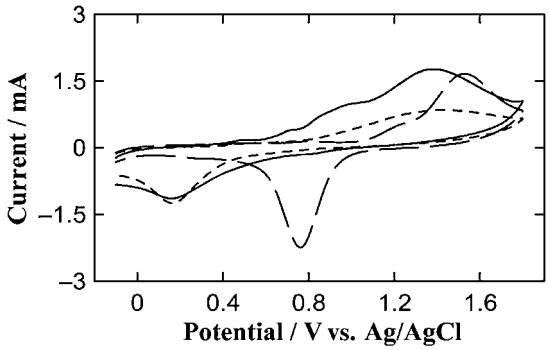

Figure 10. The cyclic voltammograms of Pd_n–BFc (dots), Au_n–BFc (dashes), and Pd_n–BFc/Au_n–BFc (solid line) films in 0.5 M aq. H_2SO_4 at 100 mV s^{-1}. The films were prepared with 75 cyclic potential scans between −0.3 and 0.9 V vs. Ag/AgCl for each metal nanoparticle layer in a solution of 3.2 μM Pd_n–BFc, or Au_n–BFc, in 0.1 M Bu_4NClO_4–CH_2Cl_2 at 100 mV s^{-1} at ITO (Ref. 56).

1.1.4 Application Examples: This electrodeposition system can be adaptable to other metals in place of gold. The adhesive films of the BFc-modified palladium nanoparticle (Pd_n–BFc)[54] were prepared by the same electrodeposition process (Pd_n–BFc could be synthesized by the thiol-exchange reaction between octanethiolate-stabilized Pd nanoparticles[55] and BFcS). The tetragonal-like aggregation of Pd_n–BFc was observed similar to Au_n–AQ. By utilizing both Pd_n–BFc and Au_n–BFc, a BFc-active composite thin film with an alternating layered structure can be fabricated (Scheme 2). First, the electrodeposition of Pd_n–BFc ($d_{av} = 3.8$ nm) is performed by potential cyclic scans, which is followed by the electrodeposition of Au_n–BFc ($d_{av} = 2.9$ nm), thus forming the Pd_n–BFc/Au_n–BFc composite film.[56] The two-step hetero-electrodeposition procedure is repeated in order to increase the number of composite layers. Figure 9 shows the XPS spectra of the composite film, displaying that the Au $4f_{5/2}$ (87.5 eV) and $4f_{7/2}$ (83.9 eV) peaks are not detected in the first layer of Pd_n–BFc, although they appear after deposition of the second layer of Au_n–BFc. In addition, the formation of the third layer of Pd_n–BFc shelters most of these Au peaks, suggesting that the prepared films build up an alternately layered structure of Pd_n–BFc and Au_n–BFc. This proves that enough electron transfer exists among heterogeneous interfaces of Pd_n–BFc and Au_n–BFc to develop a composite film gaining an average of 5 M_n–BFc (M = Pd and Au) layers above the second layer.

The interesting electrochemical properties of the Pd_n–BFc/Au_n–BFc film were observed in aq. H_2SO by CV (the Pd_n–BFc layer contacted an electrode), and the results are displayed in Figure 10. The Pd_n–BFc only film undergoes a redox process exhibiting an oxidation peak at 1.3 V, which corresponds to the formation of a palladium oxide layer on the particle surface, followed by re-reduction at 0.3 V; the Au_n–BFc only film possesses the same type of oxidation and reduction peaks at 1.6

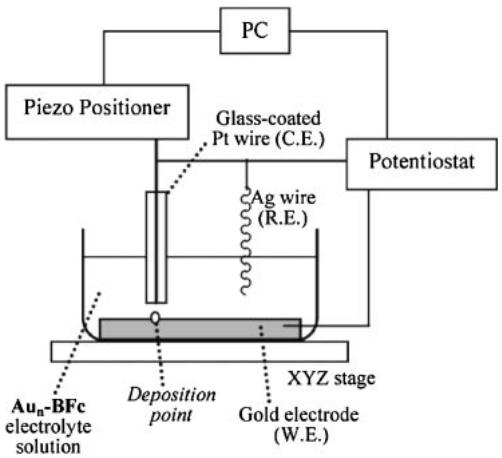

Scheme 3. Diagram of the SECM apparatus for electrodeposition of Au_n–BFc (Ref. 42).

and 0.8 V, respectively. The Pd_n–BFc/Au_n–BFc composite film exhibits an oxidation peak at 1.3 V, which can be interpreted as the collective oxidation reaction of the Pd_n–BFc and Au_n–BFc. On the other hand, the reduction peak appears at 0.3 V, which is the same potential as that of the Pd_n–BFc film, with inhibition of the reduction of the Au_n–BFc layer at 0.8 V. No appearance of the peak at 0.8 V suggests that the Pd_n–BFc layer is sufficiently conductive that it is capable of mediating the oxidation reaction of Au_n–BFc, however the electron transfer between the oxidized form of the Pd_n–BFc and Au_n–BFc films is considerably hindered. This implies that electron transfer in the metal nanoparticle films can be controlled by changing the combination of core metal elements. This system would be a typical example to elucidate electron-transfer reaction in heterogeneous metal nanoparticle films.

In another experiment, scanning electrochemical microscopy (SECM) enabled dot- and line-shape lithographic assemblies of Au_n–BFc particles at a resolution of 50–100 nm.[42] When the substrate electrode potential is kept at 1.1 V in Au_n–BFc solution where the electro-oxidative deposition of Au_n–BFc occurs, the electronic density due to the faradaic current tends to gather at the area of the substrate where the distance to the counter electrode is the closest (deposition point in Scheme 3). The CCD images of the lithographic deposition of Au_n–BFc in Figure 11 clearly illustrate the black precipitates deposited in a specific area. The simplest diagram is a "dot" described in Figure 11C, which is prepared by maintaining the deposition time of 5 s without moving the 7 μm diameter Pt counter electrode. A line drawing of Au_n–BFc deposition is possible with ca. 100 μm width deposited by moving the counter electrode (Figures 11A, 11B, 11D, and 11E). It is expected that the variable parameters, such as the distance between counter electrode and substrate electrode, the scan speed, and the counter electrode diameter, could be applied to change the line width and the deposition thickness to produce more precisely controlled shapes. These assembly systems would be also applicable by attempting to use STM and AFM instruments in place of SECM with higher lithographic resolution.

1.2 Discotic Liquid Crystalline Molecule-Modified Gold Nanoparticles with Assembly Structure Controlled by Solvent Polarity. Many studies related to the construction

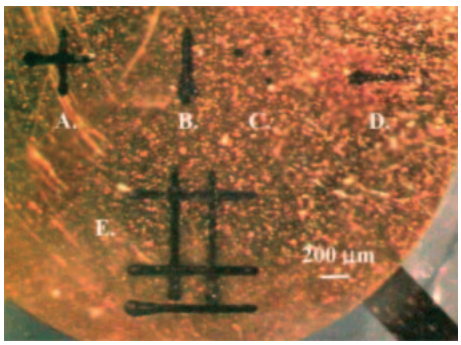

Figure 11. CCD image of the lithographic Au_n–BFc deposition on a gold electrode substrate prepared in 10 μM Au_n–BFc in 0.1 M Bu_4NClO_4–CH_2Cl_2 at the substrate potential 1.1 V by SECM apparatus. Each line was deposited by moving the Pt counter electrode in a 7 μm diameter at 122.7 μm s^{-1} for 500 μm (A, B, and D) or 900 μm (E) with 10 scans. As for part C, the deposition time was 5 s without moving the counter electrode (Ref. 42).

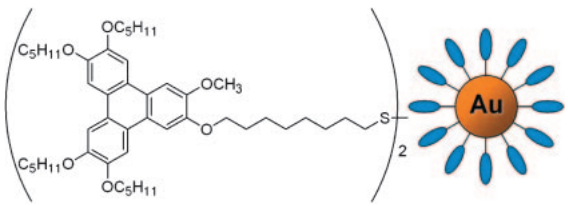

Figure 12. (Left) Structure of TPD. (Right) Schematic representation of Au_n–TP (Ref. 59).

of highly-ordered metal nanoparticle assemblies have been reported. Among them, from the viewpoint of electronic energy transport, the one-dimensional (1D) arrangement of nanoparticles is particularly interesting. The decrease in interparticle spacing can elicit a dramatic increase in particle–particle electronic interaction, leading to efficient 1D tunneling current as a role for nanowires.[57] Existing methods for fabricating the 1D arrangement of particles include the use of electron beam lithography, templates and self-assembly of nanoparticles. The self-assembly method is the most facile way by which an appropriate volume of nanoparticle solution is spread over a substrate, spontaneously constructing a thermodynamically stable arrangement of nanoparticles accompanied by solvent vaporization. However, the development of 1D assemblies is still hard to achieve, unfavorable compared to hexagonal closed packed (hcp) structure because of the low-symmetric structural isotropy. In order to accomplish the 1D assembly of nanoparticles, their structural design should be optimally refined. The secret to this research is the introduction of the discotic liquid crystal molecule, hexaalkoxy-substituted triphenylene (TP),[58] into an organic ligand surrounding a gold nanoparticle surface (Au_n–TP) (Figure 12).[59,60] TP molecules are known to self-assemble into 1D columnar mesophase via π–π interaction.[58] Consequently, it is expected that TP molecules would be a strong trigger for the 1D assembly of metal cores by introducing TP units onto metal nanoparticle surfaces.

Au_n–TP with 2.4 nm diameter was synthesized in a homogeneous reduction of $HAuCl_4$ in DMF/water with TP thiol

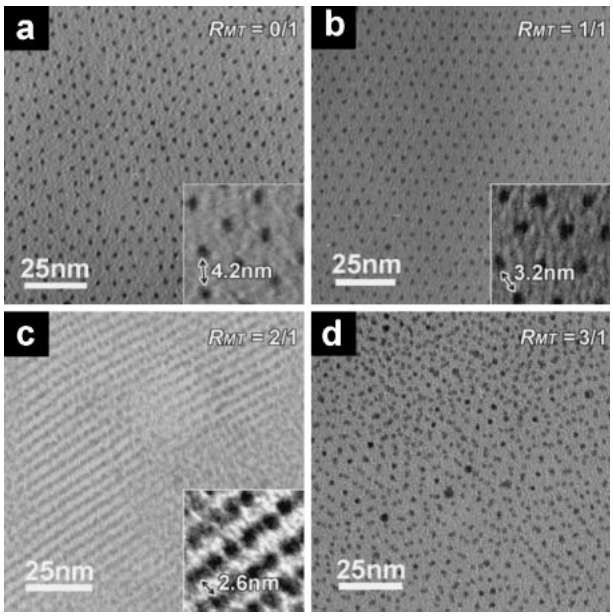

Figure 13. TEM images of Au_n–TP prepared in (a) $R_{MT} = 0/1$, (b) 1/1, (c) 2/1, and (d) 3/1. The inset shows the enlarged image (Ref. 59).

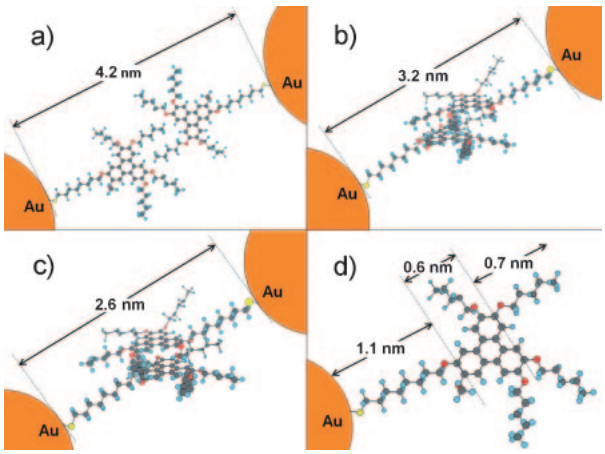

Figure 14. Schematic illustration of (a) adjacent TP ligands on a gold core surface with non-stacking ($d_{int} = 4.2$ nm), (b) with partial stacking ($d_{int} = 3.2$ nm), (c) with full stacking ($d_{row} = 2.6$ nm) of TP units, and (d) a single TP ligand on a gold core surface (Ref. 59).

derivative, bis{8-[3-methoxy-6,7,10,11-tetrakis(pentyloxy)triphenylen-2-yloxy]octyl} disulfide (TPD, Figure 12). Figure 13 shows the TEM images of the Au_n–TP assemblies prepared in a mixture of a polar (methanol) and a less polar (toluene) solvent. The solvent polarity was controlled by altering the mixed ratio of methanol to toluene (v/v), R_{MT}, from 0/1 to 3/1. The R_{MT} value is regarded as a polarity index. When the solvent polarity is relatively low ($R_{MT} = 0/1$, 1/1), a clear hcp structure is formed with particle spacing, d_{int}, of 4.2 and 3.2 nm, respectively (Figures 13a and 13b). The full molecular length of the TP ligand is ca. 2.4 nm calculated by MOPAC described in Figure 14d, where the C8 alkyl chain is 1.1 nm, the aromatic frame of the TP moiety is 0.6 nm, and the surrounding pentyloxy group of the TP moiety is 0.7 nm. Considering this physical structure of the TP ligand and the interparticle spacing of the assemble structure, the interaction among the adjacent Au_n–TPs is slightly different between Figures 13a and 13b, although they display the same hcp assembly. Namely, the Au_n–TP in Figure 13a assembles by intercalating only the adjacent pentyloxy moiety around the TP ligands (Figure 14a). On the other hand, those in Figure 13b should accompany the partial π–π interaction of TP units (Figure 14b). Interestingly, when the polarity of the solvent is further increased to $R_{MT} = 2/1$, the assembly structure is entirely converted from hcp to a 1D arrangement (Figure 13c). The interparticle spacing in a chain is ca. 0.7 nm. The row spacing, d_{row}, is 2.6 nm, a value which is consistent with the full stacking of the TP units interdigitated among the adjacent Au–TP particles (Figure 14c). The well-defined superstructure of Au_n–TP disappears with an increase of R_{MT} above 3/1 (Figure 13d).

This assembly mechanism can be explained in detail by the fluorescence spectrum of the Au_n–TP solution in methanol/toluene. With increasing time, a significant enhancement of the FL intensity at 412 and 438 nm was identified for $R_{MT} = 1/1$ (hcp) and 2/1 (1D), while it was not observed for $R_{MT} = 0/1$ (hcp) and 3/1 (disordered). Above all, the intensity increase for $R_{MT} = 2/1$ (1D) is conspicuous compared with that for $R_{MT} = 1/1$ (hcp). Considering that the emissions at 410–440 nm are attributed to the conventional staggered or helical π-electron overlapping mode of the TP molecules,[61] these FL data imply that the TP units on a particle surface are gradually intercalating among neighboring particles, and that they produce the interparticle π–π electronic stacking of the TP units. This agrees rationally with the TEM observations and MOPAC calculations. That is, the TP units generate π electronic stacking among particles most frequently with $R_{MT} = 2/1$ to give a 1D assembly with fully-overlapped TP moieties. In the same way, the TP moieties are secondarily inclined to be stacked with $R_{MT} = 1/1$, leading to hcp ordering with partially-overlapped TP moieties. This is definite evidence that the interaction among the nanoparticles in solution determine the final assembly structure on a substrate after solvent evaporation.

Similar assembly control was possible even for Au nanoparticles functionalized with another TP ligand with a C12 alkyl chain [bis{8-[3-methoxy-6,7,10,11-tetrakis(pentyloxy)triphenylen-2-yloxy]dodecyl} disulfide as shown in Figure 15.[60] This is abbreviated as Au_n–TPC12 ($d_{av} = 2.8$ nm). The assembly structure of Au_n–TPC12 was also changeable by the solvent polarity used. d_{int} in the hcp structure is ca. 4.0 nm, corresponding to the partial π–π stacking of TP units with C12 among Au_n–TPC12 (Figure 15b). Meanwhile, d_{row} in the 1D arrangement is determined as 3.4 nm, equal to the full stacking of the TP units with C12 (Figure 15c). There, the 1D arrays of AuTP–C12 are spread over up to ca. 0.5 μm long aligned in a parallel fashion.

From the results it can be deduced that the strong interparticle π–π interaction of TP units in solution is inevitable for the 1D arrangement of Au_n–TPs, while that interaction is supportive, but not indispensable for the hcp ordering of Au_n–TPs. The plausible mechanism is of course attributed to the specific nature of TP ligands that discotic liquid crystalline molecules tend to gather into a 1D column as

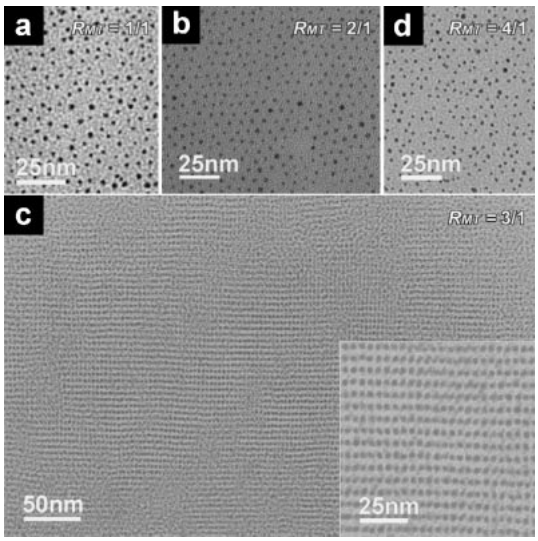

Figure 15. TEM images of Au_n–TPC12 prepared in (a) $R_{MT} = 1/1$, (b) 2/1, (c) 3/1 (inset is the enlarged image), and (d) 4/1 (Ref. 60).

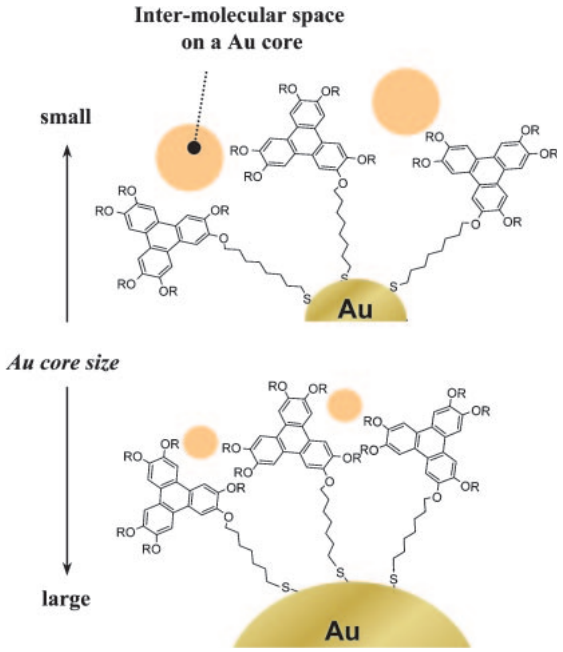

Figure 16. Illustration of relations between the core size and the intermolecular spacing of Au_n–TP.

mentioned at the beginning. When the interparticle π–π stacking is promoted in an appropriate mixed solvent, the small columnar phase of TP units will be constructed by the intercalation of TP ligands among Au_n–TPs. During the ordering process of the collected TP columnar phase, partial exposure of the metal core surface, where the protection by TP ligands becomes weak due to the alkyl chain bending of TP ligands turning to the TP column direction, is inevitably produced. Accordingly, the van der Waals attraction among the metal cores is accelerated, causing the gradual aggregation of Au_n–TPs. At that time, the specific 1D nuclei of Au_n–TPs are compulsorily constructed as a result of the surrounding TP column, leading to secondary growth of the 1D Au_n–TP arrays through directional motion of nanoparticles toward the ordered arrays, accompanied by solvent evaporation.

It should be mentioned that in order to provoke the interparticle π–π interaction of Au_n–TPs, not only the introduction of TP units onto a gold core and the adjustment of the solvent polarity, but also the precise control of the gold core are indispensable. Au_n–TPs with a different core diameter, $d_{av} = 2.4$, 2.8, and 3.0 nm, can be prepared by changing the molar ratio of Au ions to TPD in synthetic solution however only the smallest Au_n–TPs ($d_{av} = 2.4$ nm) can assemble linearly. This is explained by the reduction of inter-particle spacing among TP units on the gold cores with increasing core size resulting from the interface curvature of a core becoming more even (Figure 16),[62] leading to inhibition of intercalation of the TP units among the neighboring Au_n–TPs. This important study demonstrates that both the appropriate physical architecture of nanoparticles (both the introduction of a functional molecule and the diameter ratio of a core to shell) and the parametric balance in self-assembly are essential for the precise control of nanoparticle arrangement.

2. Morphology Control of Metal Nanoparticles as Advanced Catalysts

A large body of research up to now has pointed out that the properties of metal nanopaticles are greatly dependent on morphology. For instance, the absorption originating from the surface plasmon oscillation of gold nanoparticles is dramatically red-shifted when the nanoparticle shape changes from spherical to rod like.[63,64] Likewise the catalytic activity of metal nanoparticles increases with decreasing diameter, since the ratio of surface atoms increases exceedingly.[65] In this section, the focus is development of advanced catalysts by controlling the shape and size of metal nanoparticles. It is not simple to arrange their physical structure precisely in solution,[66,67] since various synthetic parameters e.g., temperature, time, concentration, solvent, surfactant, and organic ligand, should be considered to control free energy change (ΔG) which determines the specific shape of the resulting nanoparticles.[26] An intelligent synthetic system which controls the accurate crystal growth of metal nanoparticles both kinetically and thermodynamically should be devised by selecting appropriate parameters. Under consideration of these factors, highly shape-selective synthesis of cubic Pt nanoparticles was accomplished by means of an ionic additive. In another experiment, the preparation of gold nanoparticle catalyst with high monodispersity was useful for carbon nanotube synthesis by chemical vapor deposition (CVD).

2.1 Synthesis and Size Control of Platinum Nanocubes with High Shape Selectivity. The catalytic properties of Pt nanoparticles are expected to be useful for organic synthesis, the decomposition of exhaust gas, and polymer electrolyte fuel cells (PEFC). Fuel cells possess high energy conversion efficiency originating from the chemical energy of combustion of hydrogen and oxygen, without emitting environmental pollutants including CO_2. Among several different fuel cells, PEFC is likely to become the most common in the general community because of its low operating temperature (below 100 °C). However, to enable practical use, the cost of the Pt

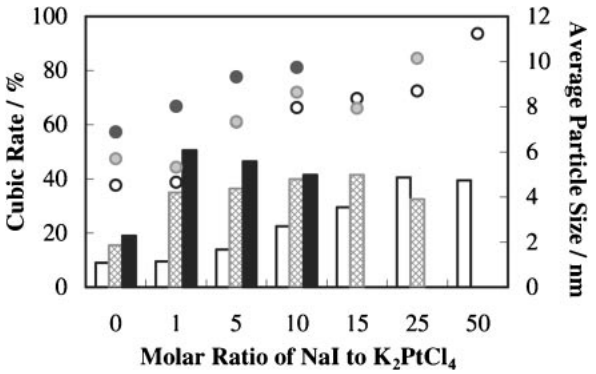

Figure 17. Effect of the NaI molar ratio to K_2PtCl_4 on the average particle size (circles) and the cubic selectivity (bars) of the prepared Pt_n–PAA. The concentration of K_2PtCl_4 was 0.1 (white), 0.5 (gray), and 1.0 mM (black), respectively (Ref. 70).

nanoparticles used as the electrode catalyst in PEFCs must be reduced, which can be accomplished by developing Pt nanoparticles with more efficient catalytic activity. Their catalytic activity is thought to depend on shape and size, and cubic Pt nanoparticles are anticipated to exhibit higher catalytic activity compared to spherical particles. This is because cubic particles are composed of only (100) facets, with more defective and active sites accompanied by dissolution and surface reconstruction than (111) facets.[68] As for particle size, around 5 nm is reported to produce the most efficient catalytic performance.[69] There are several studies which have proposed preparation methods for Pt nanocubes, however, particle size was relatively large ($>\approx$10 nm) with wide distribution.[27] Precise size control has not yet been achieved.

In order to make the cubic shape of Pt nanoparticles uniform, anion species received attention because anions are generally known to adsorb onto a Pt crystal surface, and are considered to affect the growth rate between {100} and {111} faces of Pt nanoparticles in solution. A series of experiments revealed that the additive effect of NaI enables the size and shape control of Pt nanoparticles stabilized by polyacrylic acid sodium salt (Pt_n–PAA) with cubic selectivity of up to 84%.[70] Cubic Pt_n–PAA can be prepared as follows: NaI with a predefined molar ratio to K_2PtCl_4 is dissolved in 50 mL of x mM K_2PtCl_4 and PAA aqueous solution ($x = 0.1$, 0.5, and 1, K_2PtCl_4/polyacrylic acid unit = 1), followed by the reduction of Pt ions by bubbling H_2 gas.

Pt_n–PAA was prepared both with and without NaI, which revealed that the cubic selectivity of Pt_n–PAA became apparently high when NaI coexisted in the reaction mixture. In addition, other polymers (e.g., PVP) in place of PAA did not produce Pt nanocubes, suggesting that both PAA and NaI worked synergistically adjusting the cubic shape. Further investigation of the NaI effect on the physical structure of Pt_n–PAA was carried out by changing the molar ratio of NaI to K_2PtCl_4, as summarized in Figure 17. Notably, the ratio of the cubic nanoparticles to all of the produced particles (=cubic ratio) and the average particle size tend to increase with increasing NaI ratio and Pt concentration. This result indicates the formation mechanism of the cubic Pt_n–PAA: after a particle nucleus is generated at the first stage of the reaction, the particle

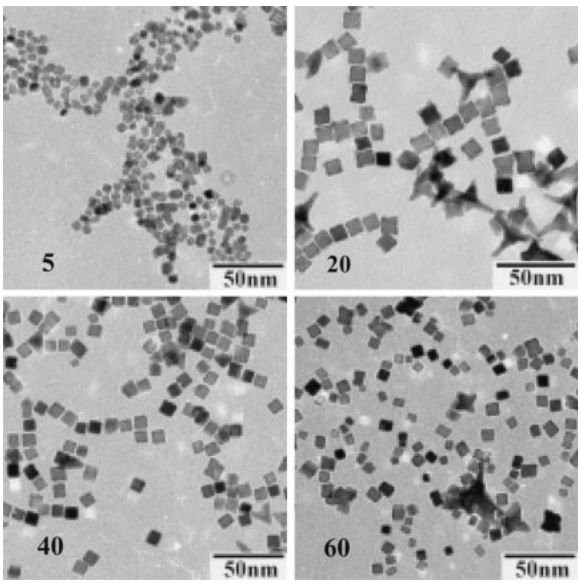

Figure 18. TEM images of Pt_n–PAA prepared with a different reaction temperature of which the value is noted in the images (Ref. 70).

crystal grows gradually, accompanied by the different growth ratios between the {111} and {100} faces under the additive effect of I^-.

Figure 18 shows TEM images of Pt_n–PAA synthesized at different reaction temperatures, T, from 5 to 60 °C. They demonstrate that the cubic Pt_n–PAA can be preferentially obtained between 20 and 60 °C with high selectivity ca. 70–80%. The cubic size is controllable between 7.5–10.5 nm by changing T. The particle size first increased with rise of T until 20 °C, and then gradually decreased. This is explained by the existence of mainly two factors which determine the particle size during the synthetic process, electrostatic repulsion and thermal energy. Considering the general equation of the electrostatic interaction (V_R) where V_R is in proportion to T, the size should decrease with increasing T. On the contrary, considering thermal energy put into the synthetic solution, metal nuclei approach closer by overcoming an energy barrier, leading to the size increase. In this case, it is thought that the former factor is predominant from $T = 20$ to 60 °C, while the latter predominates from $T = 5$ to 20 °C. It is evidenced that temperature is the most effective parameter to control the cubic size of Pt_n–PAA, maintaining high shape selectivity.

The electrochemical behavior of thus prepared Pt_n–PAA was preliminarily investigated, which indicated the catalytic activity for oxygen reduction reaction (ORR) on the cubic Pt_n–PAA was higher than that on the general sphere Pt_n–PAA. This means that the (100) facets on the cubic Pt_n–PAA work effectively for catalytic performance as expected, and additionally, the adsorption of I ions on the particle surface does not influence its catalytic activity so much. Precise examination is underway, and will be reported in the near future.

2.2 Synthesis and Diameter Control of Multi-Walled Carbon Nanotubes over Gold Nanoparticle Catalysts. The characteristics of carbon nanotubes (CNTs)[65] including electrical behavior and mechanical strength have been energetically studied for decades. Nanoparticles of 3d transition metals (Fe,

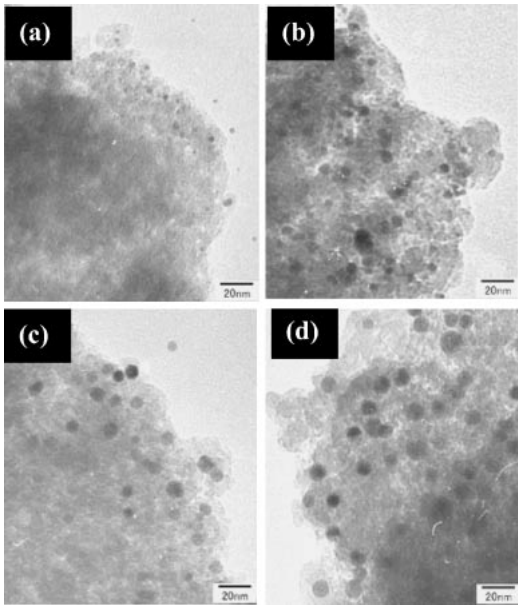

Figure 19. TEM images of (a) Au_n–DT1/SiO_2–Al_2O_3, (b) Au_n–DT2/SiO_2–Al_2O_3, (c) Au_n–DT3/SiO_2–Al_2O_3, and (d) Au_n–DT4/SiO_2–Al_2O_3 (Ref. 74).

Co, Ni, etc.) are widely used as catalysts for the synthesis of CNTs in chemical vapor deposition (CVD). Accordingly, studies of noble metal nanoparticles for CNT catalysts attract great interest. Bulk gold has long been regarded as inert and less active as a catalyst, a condition attributed to its completely filled 5d shell and the relatively high value of its first ionization, however gold begins to show interesting catalytic behavior e.g., CO oxidation, hydrocarbon oxidation, and NO reduction when its size is reduced into a nanoscale regime.[71] Here, research interests have been focused on the question whether the synthesis of multi-walled carbon nanotubes (MWNTs) over a gold nanoparticle catalyst is possible or not.[72,73]

The gold nanoparticles used as a catalyst were stabilized by dodecanethiol (DT), followed by being supported on SiO_2–Al_2O_3. First, DT-surrounded gold nanoparticles (Au_n–DT) with different core diameters of $d_{av} = 2.1$ nm (Au_n–DT1), 3.7 nm (Au_n–DT2), 5.3 nm (Au_n–DT3), and 7.0 nm (Au_n–DT4) were synthesized, and each size-controlled Au_n–DT was supported to produce the Au_n–DT/SiO_2–Al_2O_3 catalyst (0.1 wt % gold) after calcination for 1 h at 200 °C. The particle core diameter in Au_n–DT(1–4)/SiO_2–Al_2O_3 was measured at 3.0 ± 0.7, 5.0 ± 0.7, 8.3 ± 1.0, and 10.0 ± 1.1 nm, respectively (Figure 19). Comparing the values of the particle size before and after being supported, an aggregation among adjacent particles in the SiO_2–Al_2O_3 matrix occurred, leading to the ca. 1.5 times crystal growth during calcination. The particles remained separately dispersed in SiO_2–Al_2O_3, and reflected the size order of the Au_n–DT used as a starting particle. This confirms that this catalyst preparation using a size-selective nanoparticle prepared in solution is effective for managing the precise particle size in catalysts. Apparently, the size distribution becomes narrower than that obtained by general methods of nanoparticle catalysts, such as impregnation methods[74] in which metal ions dispersed into a support are reduced in a solid state.

Table 2. Dependence of a Catalyst on the Outer Diameter of the MWNTs Formed by Using C_2H_2 as a Carbon Source (Ref. 72)

Nanoparticle for a catalyst	Outer diameter of MWNTs/nm				
	450[a)]	500[a)]	550[a)]	600[a)]	700[a)]
Au_n–DT1	—[b)]	9.1	9.5	10.3	14.0
Au_n–DT2	—	—	13.0	14.3	16.5
Au_n–DT3	—	—	23.0	17.0	20.2
Au_n–DT4	—	—	—	19.3	23.3

a) Reaction temperature (°C). b) Dash indicates that no MWNTs were identified.

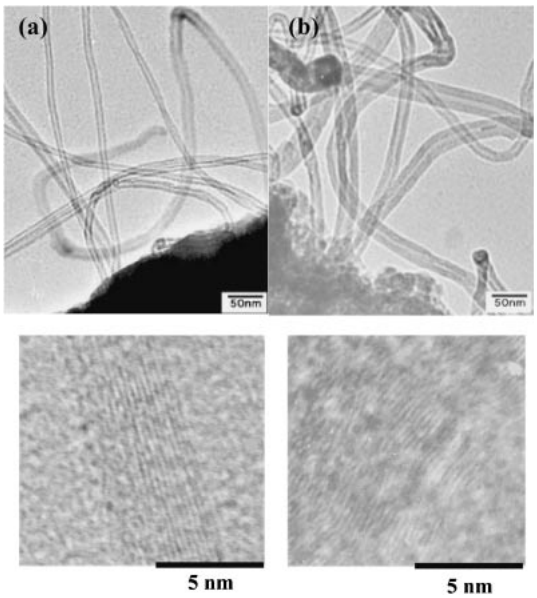

Figure 20. (Top) TEM and (bottom) HRTEM images of MWNTs formed at 600 °C by using (a) C_2H_2 (MWNT–C_2H_2) and (b) C_2H_4 (MWNT–C_2H_4) as a carbon source over Au_n–DT2/SiO_2–Al_2O_3.

The influence of reaction temperature and the size of Au_n–DT on the formation of MWNTs was investigated by using C_2H_2 as a carbon source over Au_n–DT(1–4)/SiO_2–Al_2O_3, summarized in Table 2. It shows that the outer diameter of the formed MWNTs becomes larger with an increase of the size of Au_n–DT introduced as catalyst, suggesting that gold is catalytically active for the preparation of MWNTs, and their diameter control can be carried out by the size-selective preparation of the starting nanoparticle catalyst. From another aspect, the outer diameter of MWNTs tends to increase at higher reaction temperatures, which is explained by the considerations that (1) during the reaction, the size of nanoparticles in catalysts grows gradually by heat-induced aggregation among adjacent particles, and (2) the catalytic reaction is accelerated at higher temperatures. In addition, MWNTs can be generated at lower temperatures with decreasing size of nanoparticle in catalysts, attributed to higher catalytic ability for smaller nanoparticles.

Figure 20 shows the TEM and HRTEM images of MWNTs formed at 600 °C by using (a) C_2H_2 (MWNT–C_2H_2) and (b) C_2H_4 (MWNT–C_2H_4) over Au_n–DT2/SiO_2–Al_2O_3, which dis-

plays the dependence of the physical structure of MWNTs on the carbon source. Consecutive carbon layers with interlayer ideal spacing of 0.38 nm[75] are observed in the image of MWNTs produced by C_2H_2 (MWNT–C_2H_2), while undulated layers covered by amorphous carbon are identified in that of MWNT–C_2H_4. Many unrevealed points remain concerning the mechanism of CNT formation, even over a general 3d metal catalyst; however, it is proposed that the tip- and base-growth models[76] can be also applied to a gold nanoparticle catalyst. After nucleation of CNTs at the gold nanoparticle surface, the tube growth process begins. During growth, the wall layers are created in a uniform axial direction by the introduction of C_2H_2 molecules, possessing a regular growth of the parameter values relating to the CNT diameter. On the other hand, the carbon wall grows more randomly into several axes with C_2H_4 molecules, leading to less dependence of the CNT configurations on the size of Au_n–DT. It should be mentioned that the formation of MWNTs was recognized with the introduction of C_2H_2 and C_2H_4 gases, while it was not with that of benzene and methanol. Considering that 3d metal nanoparticles exhibit catalytic activity to all of these carbon-containing molecules, these results including the discrepancy between C_2H_2 and C_2H_4 noted above indicates that the noble metal gold possesses specific catalytic activities different from general catalytic metals. The minute interpretation of catalytic reaction over gold nanoparticles is still attractive.

3. Introduction of Metal Coordination Polymers into a Nanoparticle Core

In the last section, metal coordination compounds are focused on as an inorganic core in place of metal elements. Metal coordination polymers, where transition-metal ions are bridged in three-dimensional (3D) nets by organic ligands,[77,78] are fascinating organic–inorganic hybrid materials with variable geometries and connections created by selecting appropriate bridging ligands and metal ions, leading to useful wide-ranging properties, e.g., electronic, magnetic, electrochromic, optical, catalytic, and adsorptive characteristics. The discussion about their specific nature has centered on bulk crystals (≈μm) for a long time. It has not been well clarified yet whether downsizing effects like those of metallic nanoparticles are observed for the behaviors of nanometer-sized metal coordination polymers, which have been named metal coordination nano-polymers (MCNPs).[79–84] As a first step, it is important to standardize a synthetic procedure for MCNPs in order to reveal the relationship between the physical structure and properties of MCNPs experimentally. Therefore, metal cyanometalates, M_1–CN–M_2 (M_1 = Fe, Ru, Co, Cr, Os, etc., M_2 = Fe, Co, Ni, Mn, Cr, Eu, La, Sm, etc.), Prussian blue ($M_1 = M_2$ = Fe), and its analogs[85,86] have been selected as metal coordination polymer. Because of a convenient synthetic procedure, M_1–CN–M_2 is one of the most widely-explored metal coordination polymers with various outstanding features as a bulk crystal including magnetism (photo-induced magnetism), electrochromism, and ionic conductivity. M_1–CN–M_2 MCNPs would be a standard model to demonstrate the possibility of metal coordination polymers as nanomaterials.

3.1 Synthesis and Downsizing Effect of Metal Coordination Nano-Polymers (MCNPs). The challenge of downsizing

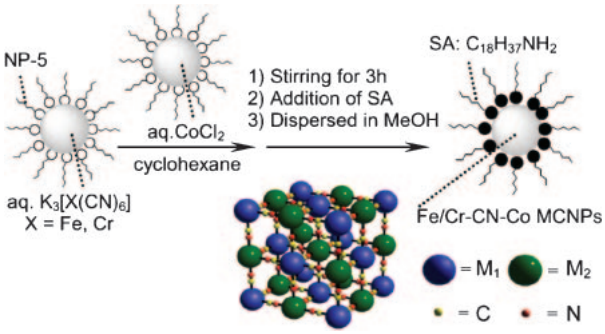

Scheme 4. Preparation of Fe/Cr–CN–Co MCNPs (Ref. 79).

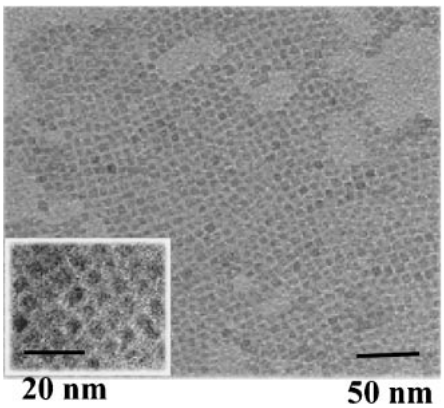

Figure 21. TEM image of SA-stabilized Fe–CN–Co MCNPs.

metal coordination polymers has appeared only in the past several years by using e.g., the reverse micelles technique,[87–89] the Langmuir–Blodgett method,[90] and inorganic template synthesis.[91] Among them, the isolation of Fe/Cr–CN–Co MCNPs (d_{av} = 5–7 nm) stabilized by an organic shell of stearylamine (SA), utilizing a reverse micelle solution of H_2O/cyclohexane/nonionic surfactant, polyethylene glycol mono 4-nonylphenyl ether (NP-5: $HO(CH_2CH_2O)_nC_6H_4C_9H_{19}$) was demonstrated.[79] The complexation between $[Fe/Cr(CN)_6]^{3-}$ anions and Co^{2+} occurs in a water nano-droplet to generate nanometer-sized crystals of Fe/Cr–CN–Co MCNPs with narrow size distribution (Scheme 4). The merits of this synthesis deserving special mention are that the prepared Fe/Cr–CN–Co MCNPs can be obtained as an air-stable powder, and the excess stearylamine is sufficiently removed during purification. The key of this isolation is the stable and strongly coordinated protection by an amine group of SA on the Co sites around the Fe/Cr–CN–Co inorganic core. Powder X-ray diffraction (XRD) patterns of the samples showed a typical face-centered cubic (fcc) structure the same as the bulk crystal, though the peaks were widely broadened due to the small crystal size. During synthesis, metal elemental control of Fe, Cr, and Co is also demonstrated by adjusting the ratio of the starting complexes in the reaction mixture. In particular, compounds comprised of only Co and Fe exhibit typical cubic shape stacked together by self-assembly (Figure 21). The value of the lattice constant, a, shifted almost linearly with increase of the Cr component, suggesting that the metal units were dispersed with high uniformity in the nano-polymers.

Figure 22. Photographs of THF solution of SA-stabilized Fe/Cr–CN–Co MCNPs. The ratio among the transition metals in synthetic solution was set as Fe:Cr:Co = 1:0:1, 3:1:4, 1:1:2, 1:3:4, and 0:1:1 from left to right in the figure (Ref. 57).

All the obtained compounds are redispersed in generally less polar solvents, e.g., CH_2Cl_2, $CHCl_3$, THF, and pyridine, due to the hydrophobic SA ligand on the nano-polymer surface (Figure 22). The solution color is dependent on elemental ratio in Fe/Cr–CN–Co MCNPs. This color variation reflects the electronic state of metal components in MCNPs, affecting their properties. For example, the compounds containing a high ratio of Cr units exhibited ferromagnetism with spontaneous magnetization at the Curie temperature. Except for nonionic NP-5, other surfactants of which the hydrophilic group is cationic (e.g., TOAB) or anionic (e.g., AOT), can be applied for this synthetic procedure.

What is the nanometer-size effect in MCNPs? In order to examine this question Cr–CN–M (M = Fe, Co, and Cu) MCNPs stabilized by the pyridine ligand, [4-(dioctadecylamino)pyridine] (OPy) were synthesized with $d_{av} = 10$–15 nm.[83] It was found that the physicochemical (shape, size, crystal structure, and electronic state) and magnetic properties were clearly different between the MCNPs and their bulk crystals dependent on the metal element M. First, the magnetic properties of Cr–CN–M (M = Fe and Co) MCNPs showed strong frequency dependence in both real (χ') and imaginary (χ'') components of alternating current (ac) magnetic susceptibility, while these components were constant for the bulk crystals. Considering both the ϕ value[92] and the relaxation time (τ),[93] this was attributed to the superparamagnetism of MCNPs with some interparticle interaction. This is the most fundamental evidence that metal coordination polymers possess a characteristic downsizing effect on their properties.

Particularly in the case of Cr–CN–Cu MCNPs, the zero field-cooled (ZFC) direct current (dc) magnetization curve possessed two separated blocking temperatures, which was not detected for the bulk crystal. This can be explained by the coexistence of several different crystal structures in Cr–CN–Cu MCNPs. From the XRD patterns, Cr–CN–Cu bulk crystal represented typical fcc structure, while Cr–CN–Cu MCNPs showed an unexpected different pattern (Figure 23). Because several peaks in the pattern of Cr–CN–Cu MCNPs appeared at positions close to those of bulk crystal, it is surmised that Cr–CN–Cu MCNPs are comprised of a crystal mixture of basic fcc structure with octahedral (O_h) Cu sites and another distorted crystalline phase originating from the non-octahedral Cu sites, e.g., tetrahedral (T_d). Generally, the coordination number of Cu^{II} ions exhibits great stereochemical plasticity by applying appropriate ligands. In particular, it is known that Cu^{II} ion prefers 2- or 4-coordinate geometry to 6-coordinate octahedral geometry in the presence

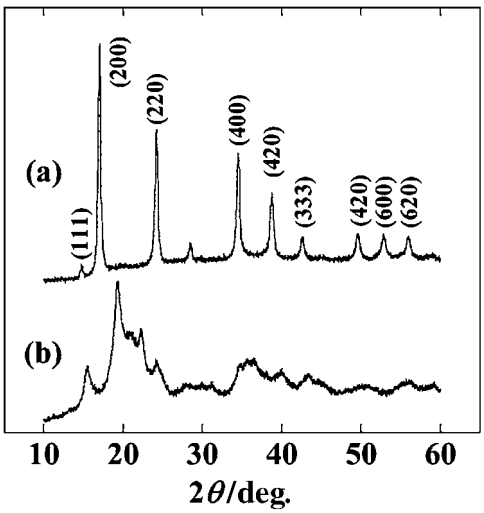

Figure 23. XRD patterns of (a) Cr–CN–Cu bulk crystal and (b) OPy-stabilized Cr–CN–Cu MCNPs (Ref. 83).

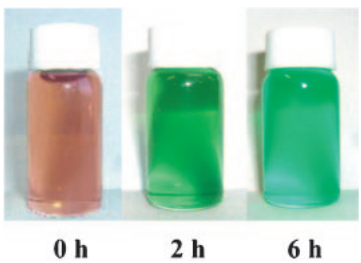

Figure 24. Photographs of Fe–CN–Co MCNPs prepared in the reverse micelle solution of CTAB during the reaction. The reaction times are noted in the figures (Ref. 81).

of bulky capping coordination ligands.[94] Therefore, it is thought that the OPy ligand acts not only as a MCNP stabilizer, but also as a capping coordination molecule for Cu sites during the reaction. As a proposed mechanism, this lattice disorder might be first induced by the strong Jahn–Teller distortion of octahedrally coordinated Cu^{II} ions in the fcc crystal system. The formed Cr–CN–Cu MCNPs are strongly influenced by OPy around their surface, which causes the conversion of the coordination geometry from $Cu^{II}(O_h)$ to $Cu^{II}(T_d)$. The coordination water of Cu sites is then released to give a distorted crystal structure. It should be mentioned that this crystal conversion did not occur by stirring both the OPy ligand and the Cr–CN–Cu bulk crystal in the same time frame. This reference experiment suggests that the interaction between the Cr–CN–Cu MCNP and the pyridine coordination group in OPy is enhanced because the ratio of surface area in MCNPs was greatly increased compared to the bulk material. A similar effect is found for the synthesis of Fe–CN–Co MCNPs in cationic reverse micelle solution of cetyltrimethylammonium halides [CTAX, X = Br and Cl].[81] The color of the reaction mixture dramatically changes from red to green with increasing reaction time (Figure 24) accompanied by a change in XRD patterns, which is due to the temporal evolution of the crystal structure from the fcc structure with $Co^{II}(O_h)$ sites to the disordered structure containing $Co^{II}(T_d)$ sites triggered by a cetyltrimethylammonium cation as a bulky capping ligand.

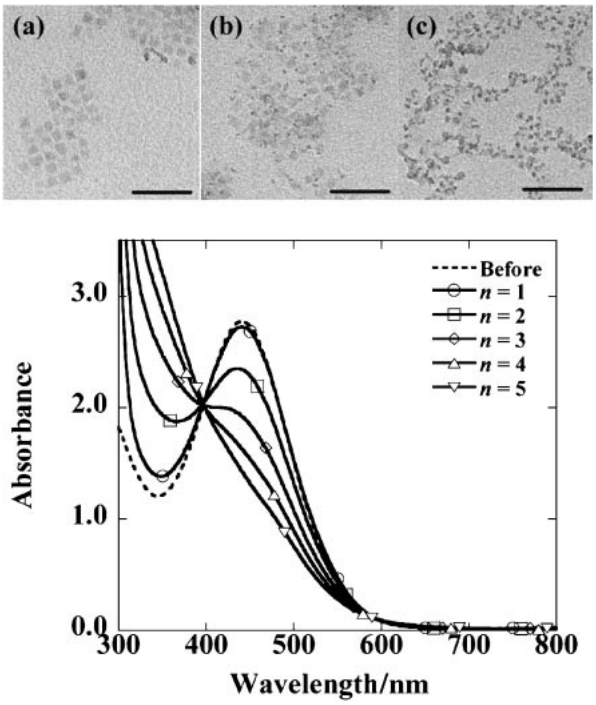

Figure 25. (Top) TEM images of OPy-stabilized Cr–CN–Fe MCNPs prepared with $n =$ (a) 1, (b) 3, and (c) 5. The scale bar is 50 nm. (Bottom) UV–vis absorption spectra of Cr–CN–Fe MCNPs in synthetic solution before and after the addition of OPy ($n = 1$–5) (Ref. 83).

These findings are examples of the surface effect of MCNPs.

Relating to the surface effect, it should be mentioned that the size and shape of Cr–CN–Fe MCNPs are dependent on the amount of the additive OPy in synthetic solution. The ratio of OPy to all of the transition metal introduced in the reaction mixture, n, was changed as 1, 2, 3, 4, and 5 (in the general procedure, n equals 1). As the value of n is increased, the number of cubic Cr–CN–Fe MCNPs ($n = 1$) is relatively reduced while producing some irregular small aggregates (Figure 25, top). Simultaneously, UV–vis absorption intensity at 440 nm, which is assigned to the intervalence charge-transfer (IVCT) band between Fe^{II}_{HS} and Cr^{III}, decreases in proportion to the value of n (Figure 25, bottom). In addition, from FT-IR spectra in the CN stretching region, the relative intensity of the higher wavenumber peak at 2160 cm^{-1} to the lower one at 2080 cm^{-1} decreases with increasing value of n (Figure 26, left). Considering that the higher and lower peaks are attributed to Cr^{III}–CN–Fe^{II}_{HS} (high spin) and Cr^{III}–NC–Fe^{II}_{LS} (low spin) respectively,[95] this is plausibly the first example of surface ligand-induced linkage isomerism. The linkage isomerism of Cr–CN–Fe accompanied by the cyano flip and the subsequent spin change is explained by the transformation of Cr^{III}–CN–Fe^{II}_{HS} to the more stable Cr^{III}–NC–Fe^{II}_{LS} on heating or standing at room temperature for several months with an obvious color change from brick red to green, which has been known for the bulk crystal of Cr–CN–Fe. As the pyridine group of OPy coordinates to the Fe^{II}_{HS} sites on the MCNP surface in place of the water molecules, the crystal field stabilization energy is enlarged to change the spin state from Fe^{II}_{HS} to Fe^{II}_{LS}. Consequently, the cyano flip occurs to switch the structure

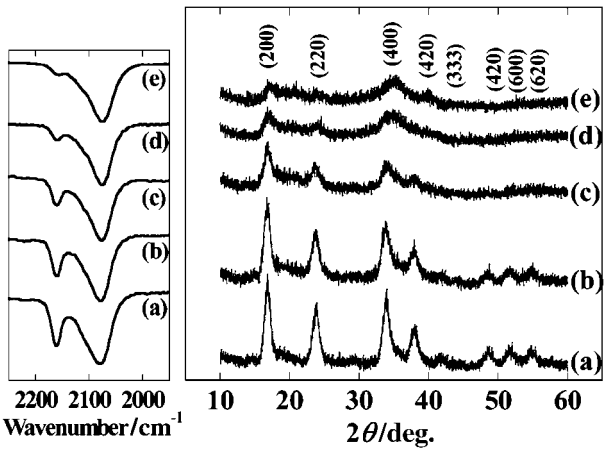

Figure 26. (Left) FT-IR spectra and (right) XRD patterns of OPy-stabilized Cr–CN–Fe MCNPs prepared with $n =$ (a) 1, (b) 2, (c) 3, (d) 4, and (e) 5 (Ref. 83).

from Cr^{III}–CN–Fe^{II}_{HS} to Cr^{III}–NC–Fe^{II}_{LS} rapidly. The effect of the surface ligand field can be enhanced by reducing the crystal size of coordination polymers, because the high ratio of surface atoms dominates the properties of MCNPs significantly.

Note that this linkage isomerism of Cr–CN–Fe is atypical. In general, this linkage isomerism follows the decrease of the lattice constant due to the loss of the antibonding e_g electrons. For example, the lattice constant of Cr–CN–Fe MCNPs stabilized by OPy ($n = 1$) varied from 10.58 to 10.21 Å after several months while keeping the basic fcc crystal structure. On the contrary, the XRD patterns of Cr–CN–Fe MCNPs dependent on the value of n displays diffraction peaks becoming broadened and flat gradually with increasing n (Figure 26, right). It can be imagined that the crystal frame of MCNPs is more fragile and compliant than that of bulk because the total number of atoms which construct one crystal is definitely small. Therefore, when the linkage isomerism of Cr–CN–Fe MCNPs is assisted by OPy from the surface, some chemical species e.g. Fe, Cr, and CN ions might be released to collapse the fundamental structure of fcc. Subsequently, many amorphous compounds comprised of these decomposed chemical substances are generated in place of the first cubic Cr–CN–Fe MCNPs, which is reasonably expected from the TEM images (Figure 25, top). In other words, this is an etching reaction of MCNPs by a surface ligand. A number of unrevealed questions concerning MCNPs might remain, and further studies are required to understand their nanotechnological science overall.

3.2 Application Examples. The concept of downsizing M_1–CN–M_2 stabilized by organic alkyl ligands with a strong coordination group to transition-metal ions e.g., amine and pyridine, enables the large scale synthesis of M_1–CN–M_2 MCNPs with high stability,[96] and widens the horizon of metal coordination compounds as novel nano-materials, of which the properties are derived from those of the bulk crystals, e.g., nano-magnets mentioned above, sensors (H_2O_2 and glucose), and electrochromism.[97] From another point, it is perceptive that MCNPs are utilized as intelligent precursors of metal alloy or ceramic nano-materials.[80,82] Metal coordination polymers have a great advantage when the various metal elements are connected by an organic ligand with uniform composition.[77]

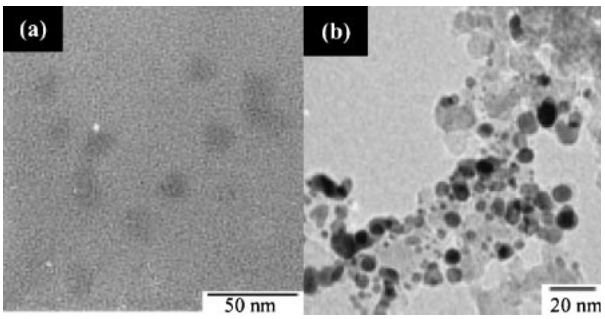

Figure 27. TEM images of SA-stabilized Pt–CN–Co MCNPs (Pt/Co = 0.9) (a) before and (b) after the transformation reaction under a H_2 atmosphere at 400 °C for 3 h (Ref. 80).

Therefore, metal coordination polymers are promising as starting precursors for inorganic materials,[98] of which the elemental composition should be precisely controlled in order to express their desirable characteristics. It is proposed that a novel synthetic approach to create metal alloy or ceramic nanoparticles by transforming MCNPs through decomposition of the bridging organic ligands of MCNPs. As for M_1–CN–M_2 MCNPs, M_1 and M_2 ions are bridged in advance by CN ligands with a regular elemental composition; M_1M_2 alloy or M_1M_2 oxide nanoparticles obtained after the decomposition reaction of CN would hold the uniform dispersion of the metal constituents with almost the same metal elemental ratio in M_1–CN–M_2 MCNPs used as starting materials. This method has several advantages in that the kinds of metal elements can be accurately introduced beforehand, and the electronic state of the nano-materials finally obtained is controllable just by altering the decomposition conditions between a reductive (H_2) and oxidative (O_2) atmosphere.

Here, the transforming process of cobalt tetracyanoplatinate (Pt–CN–Co) MCNPs through a gas-phase reduction under a H_2 atmosphere is demonstrated. SA-stabilized Pt–CN–Co MCNPs (Pt/Co = 0.9) with ca. 15-nm diameter were prepared by the complexation between $[Pt^{II}(CN)_4]^{2-}$ and Co^{2+} the same as Fe/Cr–CN–Co MCNPs (Figure 27). From thermogravimetric analysis (TGA) of Pt–CN–Co MCNPs under H_2 atmosphere, the removal of the CN ligands occurred from 350 to 450 °C with a weight loss of 24%. The X-ray photoelectron spectroscopy (XPS) spectra of Pt–CN–Co MCNPs before and after gas-phase reduction at 350 °C show that the Pt_{4f} signals at 73.1 and 76.4 eV, due to Pt^{II} sites in Pt–CN–Co MCNPs, decrease in intensity with increasing decomposition time, while new signals appear at 71.2 and 74.5 eV assigned to the metal Pt^0 (Figure 28, left). Simultaneously, the intensity of the CN stretching signal of Pt–CN–Co MCNPs in IR spectra was reduced. These results suggest that the transformation reaction from Pt–CN–Co MCNPs to PtCo alloy nanoparticles gradually occurred by the reduction of Pt and Co ions accompanied by removal of the bridging CN ligands. When reaction time is fixed at 3 h, a higher reaction temperature in the range of 350 to 450 °C could promote faster metallization reaction of Pt^{II} (Figure 28, right).

The XRD pattern of Pt–CN–Co MCNPs after the transformation reaction (at 400 °C with 3 h) exhibits an fcc structure

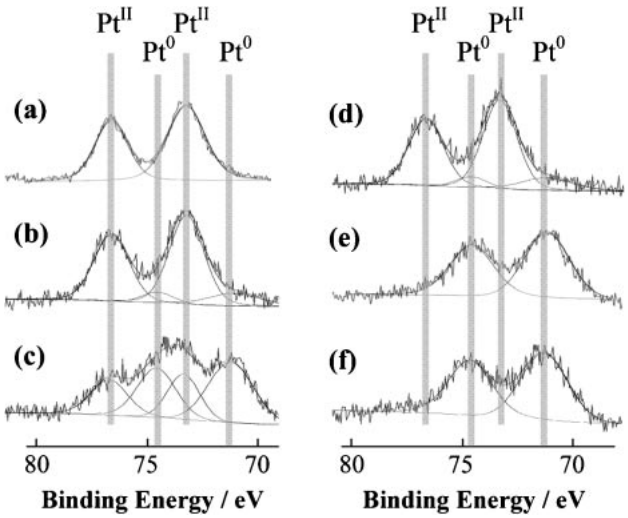

Figure 28. XPS curve in the Pt_{4f} energy range of SA-stabilized Pt–CN–Co MCNPs (Pt/Co = 0.9) before (a) and after the transformation reaction under a H_2 atmosphere at 350 °C for 3 h (b), (d), at 350 °C for 5 h (c), at 400 °C for 3 h (e), and at 450 °C for 3 h (f) (Ref. 80).

Table 3. Pt/Co Ratio and the Lattice Constant of Pt–CN–Co MCNPs (Ref. 80)

Pt/Co (cal.)[a)]	Pt/Co (anal.)[b)]	Lattice constant a/Å[c)]
1	0.9	3.76
2	1.6	3.83
3	2.9	3.86
5	3.6	3.88

a) The mixed ratio of the starting complexes. b) Determined by EDX. c) Calculated from the XRD results.

consistent with that of PtCo alloy. In the TEM image of Pt–CN–Co MCNPs after the reaction, most particles have a diameter below 10 nm (Figure 27b). The particle size is reduced compared to that of the starting Pt–CN–Co MCNPs (Figure 27a), which is due to shrinkage occurring by removal of the bridging CN between Pt and Co ions. The value of Pt/Co in Pt–CN–Co MCNPs is changeable by inserting $Pt^{IV}Cl_6^{2-}$ ions in place of Co^{2+} in reaction solution (Pt/Co = 0.9, 1.6, 2.9, and 3.6). In the XRD patterns, the diffraction peaks are shifted to lower diffraction angles almost linearly, meaning that the lattice constant, a, calculated by the XRD patterns increases almost linearly with an increase of the Pt component in the compound, suggesting that the metal components are well dispersed in a PtCo alloy nanoparticles (Table 3). Using the same method, GeFe nanoparticles with a $B8_2$ type structure (η phase) could be composed from iron tetraoxalate–germanium MCNPs and exhibited unique ferromagnetism.[82]

It was illustrated that the uniformity of metal units in MCNPs played an important role for the fabrication of versatile nanomaterials. With further development, the facile preparation of alloy/ceramic nanomaterials with novel metal elemental composition (e.g., doping several percentages of noble metal elements into the transition metals, or vice versa) will be possible, resulting in unprecedented behavior of catalytic,

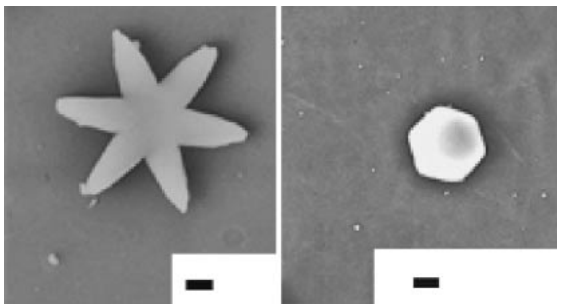

Figure 29. (Left) Fe–CN–Sm and (right) Fe–CN–Nd nanoparticles with specific shapes. The scale bar is 200 nm.

magnetic, and electronic activities. Additionally, the shape control of MCNPs e.g., cubic, asterisk, wire, film, can be carried out by contriving a synthetic procedure (Figure 29).[99] By using MCNPs with a specific physical structure as precursor, alloy/ceramic nanomaterials with unusual shapes could be fabricated after the transforming reaction. Precise investigation of these possibilities is in progress.

Conclusion

Novel organic-shell inorganic-core hybrid nanoparticles were synthesized by introducing metal or metal coordination compounds as an inorganic core. In favor of drawing out the advantages of the combination of organic and inorganic substances, suitable design of their construction is inevitable by tuning the principal parameters of unit selection, physical structure, and component ratio between inorganic and organic materials. In the first section, metal nanoparticles with additional functionalities have been created by attaching organic molecules with a multiple redox moiety (biferrocene and anthraquinone) and liquid crystalline properties (triphenylene) onto a surface of the inorganic metal core through coordination bonds by thiolate. External stimuli such as electric field and solvent polarity were utilized to transform the properties of organic molecules, leading to control of the characteristics of organic-shell inorganic-core nanoparticles. In the second, the catalytic activities of noble metal nanoparticles were investigated from the point of controlling these activities by their physical structure of shape and size. Cubic PAA-protected Pt nanoparticles were selectively prepared by addition of I^- anions to give a Pt nanocube surrounded by (100) facets with high catalytic activity for O_2 reduction. Other experiments clarified the correlation between the diameter of Au particles and that of synthesized carbon nanotubes (CNT) by changing the size of Au nanoparticle catalysts. The last section was allocated to achievements with novel nanomaterials using metal coordination polymers as an inorganic core. The metal coordination nano-polymers (MCNPs) of Prussian blue and its analogs (M_1–CN–M_2) stabilized by alkyl ligands with a coordination group to transition metals (amine and pyridine) were stable in air and obtained as a solid powder. They exhibited unusual physicochemical and magnetic properties different from their bulk crystals derived from a downsizing effect. Pt–CN–Co MCNPs could be utilized as an intelligent precursor of PtCo alloy nanomaterials after the decomposition of organic species under a H_2 atmosphere with heating. This typical reaction illustrates a promising potential that this method would be a novel method in general to fabricate particular alloy/ceramic materials on a nanometer scale with controlled shape and unequalled metal composition. Nanoparticle science in wet processes is progressing from the points of investigation of novel synthetic techniques and specialized nature, fabrication of dimensional networks, and combination of basic and applied research including miniature hardware to conduct nanoparticle behaviors. All of these studies would be connected to both the discovery of a new nano-science world and wide practical use of nanoparticle materials in the time to come.

The described studies were carried out at the University of Tokyo, Japan Advanced Institute of Science and Technology (JAIST), and Tokyo University of Agriculture and Technology (TAT). The author thanks Prof. H. Nishihara at the University of Tokyo, Prof. M. Miyake at JAIST, and Prof. M. Sakamoto and Prof. M. Kurihara at Yamagata University for the research contents. Dr. N. J. Suematsu is also thanked for his clerical assistance in completing this paper. Some parts of the presented studies were financially supported by Grants-in-Aid for Precursory Research for Embryonic Science and Technology (PRESTO) from Japan Science and Technology Agency (JST) and Grant-in-Aid for Scientific Research (Nos. 02J07874, 16710069, and 20710069) from the Ministry of Education, Culture, Sports, Science and Technology, Japan.

References

1 G. Schmid, *Chem. Rev.* **1992**, *92*, 1709.
2 G. Schmid, *Nanoparticles—From Theory to Application*, WILEY-VCH Verlag GmbH & Co. KGaA, Weinheim, **2004**.
3 M. Faraday, *Philos. Trans. R. Soc. Lond.* **1857**, *147*, 145.
4 U. Kreibig, L. Genzel, *Surf. Sci.* **1985**, *156*, 678.
5 K. A. Pettigrew, Q. Liu, P. P. Power, S. M. Kauzlarich, *Chem. Mater.* **2003**, *15*, 4005.
6 J. M. Thomas, B. F. G. Johnson, R. Raja, G. Sankar, P. A. Midgley, *Acc. Chem. Res.* **2003**, *36*, 20.
7 C. A. Mirkin, R. L. Letsinger, R. C. Mucic, J. J. Storhoff, *Nature* **1996**, *382*, 607.
8 H. Wang, D. W. Brandl, P. Nordlander, N. J. Halas, *Acc. Chem. Res.* **2007**, *40*, 53.
9 S. Sun, C. B. Murray, D. Weller, L. Folks, A. Moser, *Science* **2000**, *287*, 1989.
10 M.-C. Daniel, D. Astruc, *Chem. Rev.* **2004**, *104*, 293.
11 G. Schmid, R. Pfeil, R. Bœse, F. Bandermann, S. Meyer, G. H. M. Calis, J. W. A. van der Velden, *Chem. Ber.* **1981**, *114*, 3634.
12 G. Schmid, *Polyhedron* **1988**, *7*, 2321.
13 N. Toshima, T. Takahashi, H. Hirai, *J. Macromol. Sci., Part A* **1988**, *25*, 669.
14 M. Brust, M. Walker, D. Bethell, D. J. Schiffrin, R. Whyman, *Chem. Commun.* **1994**, 801.
15 B. A. Korgel, S. Fullam, S. Connolly, D. Fitzmaurice, *J. Phys. Chem. B* **1998**, *102*, 8379.
16 N. Toshima, M. Harada, Y. Yamazaki, K. Asakura, *J. Phys. Chem.* **1992**, *96*, 9927.
17 M. J. Hostetler, C.-J. Zhong, B. K. H. Yen, J. Anderegg, S. M. Gross, N. D. Evans, M. Porter, R. W. Murray, *J. Am. Chem. Soc.* **1998**, *120*, 9396.
18 R. B. Khomane, A. Manna, A. B. Mandale, B. D. Kulkarni,

Langmuir **2002**, *18*, 8237.
19 T. Hyeon, S. S. Lee, J. Park, Y. Chung, H. B. Na, *J. Am. Chem. Soc.* **2001**, *123*, 12798.
20 S.-J. Park, S. Kim, S. Lee, Z. G. Khim, K. Char, T. Hyeon, *J. Am. Chem. Soc.* **2000**, *122*, 8581.
21 V. F. Puntes, K. Krishnan, A. P. Alivisatos, *Top. Catal.* **2002**, *19*, 145.
22 R. K. Baldwin, K. A. Pettigrew, E. Ratai, M. P. Augustine, S. M. Kauzlarich, *Chem. Commun.* **2002**, 1822.
23 H. Bönnemann, W. Brijoux, H.-W. Hofstadt, T. O.-Ely, W. Schmidt, B. Waßmuth, C. Weidenthaler, *Angew. Chem., Int. Ed.* **2002**, *41*, 599.
24 S. Vaucher, M. Li, S. Mann, *Angew. Chem., Int. Ed.* **2000**, *39*, 1793.
25 T. Teranishi, S. Hasegawa, T. Shimizu, M. Miyake, *Adv. Mater.* **2001**, *13*, 1699.
26 J. Cheon, Y.-W. Jun, S.-M. Lee, in *Nanoparticles: Building Blocks for Nanotechnology*, ed. by V. Rotello, Plenum Publishers, New York, **2004**, pp. 53–87.
27 C. Burda, X. Chen, R. Narayanan, M. A. El-Sayed, *Chem. Rev.* **2005**, *105*, 1025.
28 M. J. Hostetler, S. J. Green, J. J. Stokes, R. W. Murray, *J. Am. Chem. Soc.* **1996**, *118*, 4212.
29 T. Horikoshi, M. Itoh, M. Kurihara, K. Kubo, H. Nishihara, *J. Electroanal. Chem.* **1999**, *473*, 113.
30 P. V. Kamat, S. Barazzouk, S. Hotchandani, *Angew. Chem., Int. Ed.* **2002**, *41*, 2764.
31 M. Yamada, A. Kuzume, M. Kurihara, K. Kubo, H. Nishihara, *Chem. Commun.* **2001**, 2476.
32 A. Dawson, P. V. Kamat, *J. Phys. Chem. B* **2000**, *104*, 11842.
33 Q. Zhou, S. Wang, X. Fan, R. Advincula, J. Mays, *Langmuir* **2002**, *18*, 3324.
34 A. C. Templeton, M. J. Hostetler, E. K. Warmoth, S. Chen, C. M. Hartshorn, V. M. Krishnamurthy, M. D. E. Forbes, R. W. Murray, *J. Am. Chem. Soc.* **1998**, *120*, 4845.
35 D. I. Gittins, D. Bethell, D. J. Schiffrin, R. J. Nichols, *Nature* **2000**, *408*, 67.
36 A. C. Templeton, D. E. Cliffel, R. W. Murray, *J. Am. Chem. Soc.* **1999**, *121*, 7081.
37 M. Okuno, K. Aramaki, H. Nishihara, *J. Electroanal. Chem.* **1997**, *438*, 79.
38 T. Horikoshi, K. Kubo, H. Nishihara, *J. Chem. Soc., Dalton Trans.* **1999**, 3355.
39 M. Yamada, T. Tadera, K. Kubo, H. Nishihara, *J. Phys. Chem. B* **2003**, *107*, 3703.
40 M. Yamada, H. Nishihara, *Eur. Phys. J. D* **2003**, *24*, 257.
41 G. Sauerbrey, *Z. Phys. A* **1959**, *155*, 206.
42 M. Yamada, H. Nishihara, *Langmuir* **2003**, *19*, 8050.
43 P. V. Kamat, *J. Phys. Chem. B* **2002**, *106*, 7729.
44 N. Malikova, I. Pastoriza-Santos, M. Schierhorn, N. A. Kotov, L. M. Liz-Marzán, *Langmuir* **2002**, *18*, 3694.
45 Y.-S. Shon, G. B. Dawson, M. Porter, R. W. Murray, *Langmuir* **2002**, *18*, 3880.
46 A. J. Haes, R. P. van Duyne, *J. Am. Chem. Soc.* **2002**, *124*, 10596.
47 G. Mie, *Ann. Phys.* **1908**, *330*, 377.
48 Y.-N. Hwang, D. H. Jeong, H. J. Shin, D. Kim, S. C. Jeoung, S. H. Han, J.-S. Lee, G. Cho, *J. Phys. Chem. B* **2002**, *106*, 7581.
49 M. Yamada, H. Nishihara, *ChemPhysChem* **2004**, *5*, 555.
50 A. C. Templeton, J. J. Pietron, R. W. Murray, P. Mulvaney, *J. Phys. Chem. B* **2000**, *104*, 564.
51 M. Yamada, T. Tadera, K. Kubo, H. Nishihara, *Langmuir* **2001**, *17*, 2363.
52 K. Nishiyama, A. Kubo, I. Taniguchi, M. Yamada, H. Nishihara, *Electrochemistry* **2001**, *69*, 980.
53 M. Yamada, K. Kubo, H. Nishihara, *Chem. Lett.* **1999**, 1335.
54 M. Yamada, I. Quiros, J. Mizutani, K. Kubo, H. Nishihara, *Phys. Chem. Chem. Phys.* **2001**, *3*, 3377.
55 I. Quiros, M. Yamada, K. Kubo, J. Mizutani, M. Kurihara, H. Nishihara, *Langmuir* **2002**, *18*, 1413.
56 M. Yamada, H. Nishihara, *Chem. Commun.* **2002**, 2578.
57 V. Berry, R. F. Saraf, *Angew. Chem., Int. Ed.* **2005**, *44*, 6668.
58 D. Adam, P. Schuhmacher, J. Simmerer, L. Häussling, K. Siemensmeyer, K. H. Etzbach, H. Ringsdorf, D. Haarer, *Nature* **1994**, *371*, 141.
59 M. Yamada, Z. Shen, M. Miyake, *Chem. Commun.* **2006**, 2569.
60 Z. Shen, M. Yamada, M. Miyake, *J. Am. Chem. Soc.* **2007**, *129*, 14271.
61 M. Ikeda, M. Takeuchi, S. Shinkai, *Chem. Commun. (Camb.)* **2003**, 1354.
62 This was proven by the ^{1}H NMR spectra of Au_n–TPs, which exhibited proton chemical shift in the aromatic frame and the resonances for methoxy groups of TP units (ca. 4 ppm) on a gold core dramatically moved upfield with increasing core size, implying increase of the stacking interaction among the packed TP moieties on the core surface. That is, the smaller metal cores can reduce electronic stacking of the neighboring TP units on a metal core surface, which can maintain a sufficient space around each TP unit.
63 S. Link, M. A. El-Sayed, *J. Phys. Chem. B* **1999**, *103*, 8410.
64 M. Suzuki, Y. Niidome, Y. Kuwahara, N. Terasaki, K. Inoue, S. Yamada, *J. Phys. Chem. B* **2004**, *108*, 11660.
65 T. Saito, S. Ohshima, W.-C. Xu, H. Ago, M. Yumura, S. Iijima, *J. Phys. Chem. B* **2005**, *109*, 10647.
66 D. V. Talapin, J. H. Nelson, E. V. Shevchenko, S. Aloni, B. Sadtler, A. P. Alivisatos, *Nano Lett.* **2007**, *7*, 2951.
67 Z. Shen, M. Yamada, M. Miyake, *Chem. Commun.* **2007**, 245.
68 R. Narayaman, M. A. El-Sayed, *J. Am. Chem. Soc.* **2004**, *126*, 7194.
69 P. Stonehart, *J. Appl. Electrochem.* **1992**, *22*, 995.
70 M. Yamada, S. Kon, M. Miyake, *Chem. Lett.* **2005**, *34*, 1050.
71 M. Okumura, T. Akita, M. Haruta, *Catal. Today* **2001**, *74*, 265.
72 M. Yamada, M. Kawana, M. Miyake, *Appl. Catal., A* **2006**, *302*, 201.
73 S.-Y. Lee, M. Yamada, M. Miyake, *Carbon* **2005**, *43*, 2654.
74 G. Merenyi, J. Lind, X. Shen, T. E. Eriksen, *J. Phys. Chem.* **1990**, *94*, 748.
75 S. C. Lyu, T. J. Lee, C. W. Yang, C. J. Lee, *Chem. Commun.* **2003**, 1404.
76 S. Amelinckx, X. B. Zhang, D. Bernaerts, X. F. Zhang, V. Ivanov, J. B. Nagy, *Science* **1994**, *265*, 635.
77 J. Veciana, C. Rovira, D. B. Amabilino, *Supramolecular Engineering of Synthetic Metallic Materials*, Kluwer Academic Publishers, Dordrecht, The Netherlands, **1998**.
78 A. F. Welles, *3D Nets and Polyhedra*, Wiley-Interscience,

New York, **1977**.
79 M. Yamada, M. Arai, M. Kurihara, M. Sakamoto, M. Miyake, *J. Am. Chem. Soc.* **2004**, *126*, 9482.
80 M. Yamada, M. Maesaka, M. Kurihara, M. Sakamoto, M. Miyake, *Chem. Commun.* **2005**, 4851.
81 M. Yamada, T. Sato, M. Miyake, Y. Kobayashi, *J. Colloid Interface Sci.* **2007**, *315*, 369.
82 M. Yamada, R. Ohkawa, M. Miyake, *IEEJ Trans. C* **2007**, *127*, 1342.
83 M. Arai, M. Miyake, M. Yamada, *J. Phys. Chem. C* **2008**, *112*, 1953.
84 M. Yamada, *Organic Shell–Inorganic Core Hybrid Nanoparticles with Advanced Functions Designed by Wet Process* in *Nanoparticle: New Research*, Nova Publishers, Inc. NY, U.S.A. **2008**, Chap. 3.
85 O. Sato, S. Hayami, Y. Einaga, Z.-Z. Gu, *Bull. Chem. Soc. Jpn.* **2003**, *76*, 443.
86 S. Ferlay, T. Mallah, R. Ouahès, P. Vellet, M. Verdaguer, *Nature* **1995**, *378*, 701.
87 S. Vaucher, J. Fielden, M. Li, E. Dujardin, S. Mann, *Nano Lett.* **2002**, *2*, 225.
88 N. Kondo, A. Nakajima, Y. Sasaki, M. Kurihara, M. Yamada, M. Miyake, F. Mizukami, M. Sakamoto, *Chem. Lett.* **2006**, *35*, 1302.
89 N. Kondo, A. Yokoyama, M. Kurihara, M. Sakamoto, M. Yamada, M. Miyake, T. Ohsuna, H. Aono, Y. Sadaoka, *Chem. Lett.* **2004**, *33*, 1182.
90 J. T. Culp, J.-H. Park, I. O. Benitez, Y.-D. Huh, M. W. Meisel, D. R. Talham, *Chem. Mater.* **2003**, *15*, 3431.
91 J. M. Domínguez-Vera, E. Colacio, *Inorg. Chem.* **2003**, *42*, 6983.
92 W. E. Buschmann, J. Ensling, P. Gütlich, J. S. Miller, *Chem.—Eur. J.* **1999**, *5*, 3019.
93 G. Zhao, J.-J. Feng, Q.-L. Zhang, S.-P. Li, H.-Y. Chen, *Chem. Mater.* **2005**, *17*, 3154.
94 R. G. Wilkins, *Kinetics and Mechanism of Reactions of Transition Metal Complexes*, 2nd ed., Wiley VCH, New York, **1991**.
95 E. Reguera, J. A. Bertrán, L. Nuñez, *Polyhedron* **1994**, *13*, 1619.
96 A. Gotoh, H. Uchida, M. Ishizaki, T. Satoh, S. Kaga, S. Okamoto, M. Ohta, M. Sakamoto, T. Kawamoto, H. Tanaka, M. Tokumoto, S. Hara, H. Shiozaki, M. Yamada, M. Miyake, M. Kurihara, *Nanotechnology* **2007**, *18*, 345609.
97 S. Hara, H. Tanaka, T. Kawamoto, M. Tokumoto, M. Yamada, A. Gotoh, H. Uchida, M. Kurihara, M. Sakamoto, *Jpn. J. Appl. Phys.* **2007**, *46*, L945.
98 M. Sakamoto, K. Matsuki, R. Ohsumi, Y. Nakayama, Y. Sadaoka, S. Nakayama, N. Matsumoto, H. Okawa, *J. Ceram. Soc. Jpn.* **1992**, *100*, 1211.
99 As reference data. The compounds were prepared by mixing 35 mL of H_2O/MeOH solution (v/v = 2:5) of 0.45 M CH_3COOH and 5.7 mM $Ln(NO_3)_3$ (Ln = Sm and Nd) with 2 mL of MeOH solution of 0.1 M $(Et_4N)_3[Fe(CN)_6]$ at room temperature for 2.5 h.

Mami Yamada was born in Tokyo on April 8, 1974 and received her B.S. in chemistry from Keio University in 1998. She graduated as a Doctor of Science from the University of Tokyo in 2003. During her doctoral studies, she was also a Research Fellow of the Japan Society for the Promotion of Science (JSPS). She was appointed as an assistant professor to the Japan Advanced Institute of Science and Technology (JAIST), Ishikawa. In 2006, she moved back to Tokyo, and obtained the current position as Associate Professor at Tokyo University of Agriculture and Technology (TAT) where she leads a group of inorganic chemistry in the Department of Applied Chemistry. She has since 2006 also been a researcher at Precursory Research for Embryonic Science and Technology (PRESTO) of the Japan Science and Technology Agency (JST). Her research evolves around the development and interpretation of synthetic procedures of novel organic–inorganic hybrid nanoparticles in chemical solution, accompanied by the investigation of their characteristics.